

Continuous quantum measurement and conditional spin-squeezing in Alkali atoms

JM Geremia, John K. Stockton, and Hideo Mabuchi
 Physics and Control & Dynamical Systems, California Institute of Technology, Pasadena, CA 91125
 (Dated: December 20, 2018)

Continuous measurement of collective atomic spin by an off-resonant optical probe can produce conditional spin-squeezing, the degree of which is limited by the signal-to-noise ratio of the measurement. Here, we relate the amount of achievable squeezing to characteristic experimental parameters including the number of atoms, the volume they occupy, the intensity and detuning of the optical probe field, and the measurement duration. Our approach combines techniques from filtering theory with an analysis of the atom-probe scattering physics based on a semiclassical treatment of the atoms. From this framework, we develop a calibration of conditional spin-squeezing and demonstrate the procedure for computing it using laboratory squeezing data.

PACS numbers: 03.65.Ta, 42.50.Lc, 02.30.Yy

I. INTRODUCTION

Information gained by performing measurements on a quantum system can reduce uncertainty about one or more of its physical observables. It is, however, a basic property of quantum mechanics that measurements are invasive in the sense that they necessarily degrade one's ability to make subsequent predictions about the values of complementary observables [1]. This type of disturbance is often termed measurement backaction. In a special class of "backaction evading" experimental scenarios, however, it is possible to channel the disturbance into observables that are decoupled from the quantities of interest. When such measurements are performed with minimal technical imperfection on systems whose initial preparations are sufficiently pure, it is possible to create squeezed states through the complementary effects of information gain and measurement backaction.

This strategy provides the essential motivation for spin squeezing [2] experiments based on quantum nodemission measurement [1, 3, 4] with Alkali atoms [5, 6, 7, 8]. In such experiments, one considers a spin-polarized atomic system described by the collective angular momentum,

$$\hat{F} = \sum_{i=1}^N \hat{f}_i^{\dagger} \hat{f}_i \quad (1)$$

In this expression, $N = 1$ represents the number of atoms in the sample and $\hat{f}_i = \hat{\uparrow}_{i-1} \hat{f} \hat{\uparrow}_{i+1}$ is the total angular momentum operator for the i^{th} atom. Under physical conditions that preserve particle-exchange symmetry, the collective spin of the atomic sample can be restricted [9] to its maximum angular momentum shells such that the eigenstates, $|F; M_i\rangle$, of the collective atomic system are characterized by $\hat{F}^2 |F; M_i\rangle = \sim^2 F (F+1) |F; M_i\rangle$, where $F = N f$, for atoms with individual spin quantum number, f .

It is natural to envision the state of such a system as a classical magnetization vector, $\mathbf{F} = [F_x; F_y; F_z]$, with transverse quantum uncertainty, $\mathbf{F}_?$, as depicted in Fig. 1(A). In perfect knowledge of the orientation of \mathbf{F} arises from the unavoidable fact that the quantum operators, \hat{F}_x, \hat{F}_y and \hat{F}_z , associated with the cartesian components of \mathbf{F} fail to commute, $[\hat{F}_i; \hat{F}_j] = i\hbar\epsilon_{ijk}\hat{F}_k$. When, for example, the atoms are polarized along the laboratory x -axis, the magnetization vector assumes the value, $\mathbf{F} = [F; 0; 0]$. Its y - and z -components are both zero; however, the transverse uncertainties, $\mathbf{F}_? = [F_y; F_z]$, cannot vanish because the Heisenberg-Robertson relation,

$$\hbar \hat{F}_y^2 \leq F_z^2 \quad \frac{1}{4} \sim^2 \hbar^2 \hat{F}_x \hat{F}_y^2; \quad (2)$$

must remain satisfied. These uncertainties have the experimental implication that a statistical ensemble of z -component measurements performed on similarly prepared x -polarized atomic samples yields a measurement outcome distribution with variance F_z^2 .

In the absence of entanglement [10] between different atoms, minimum uncertainty is achieved by a coherent spin state, characterized by equal transverse variances, $F_y^2 = F_z^2 = F^2 = \sim^2$, as depicted by the circular uncertainty diagram in Fig. 1(B). Any reduction in F_z from its coherent state value must be accompanied by an increase in F_y to remain consistent with Eq. (2). Such

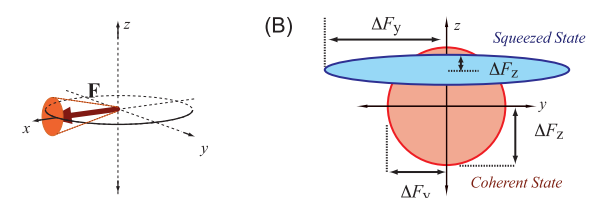


FIG. 1: (color online) (A) Graphical representation of the spin-polarized atomic sample as a classical magnetization vector with transverse quantum uncertainty. (B) Schematic of the transverse quantum uncertainties for coherent and squeezed spin states.

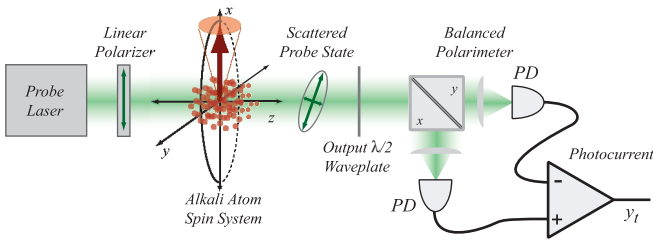


FIG. 2: (color online) Schematic of an experimental apparatus for continuous measurement of collective spin in an alkali atom sample based on polarimetric detection of a forward scattered probe laser. Information gained from the measurement can be used to achieve conditional spin squeezing.

spin-squeezed states [2] are characterized by an elliptical uncertainty diagram, as illustrated in Fig. 1(B), and are considered important for their utility in quantum information science [10, 11] and spin resonance-based precision metrology [8, 12, 13, 14, 15].

Conditional spin-squeezing experiments [5, 6, 7, 8] operate on the principle that weakly measuring F_z gradually reduces its uncertainty below that of the coherent state. The architecture typical of such procedures is diagrammed in Fig. 2. Continuous measurement of F_z is implemented by passing a linearly polarized probe laser through an atomic sample prepared into an initial (approximate) coherent state [16] by optical pumping [17]. Qualitatively speaking, the atoms exhibit state-dependent optical activity and rotate the probe polarization by an amount proportional to F_z [18]. More accurately, the optical probe field and atoms become entangled [19] as the result of a scattering interaction between them. Detecting the scattered probe field therefore yields information about F_z via this entanglement [20, 21, 22, 23, 24].

Naturally, spin-squeezing experiments aim to achieve as much uncertainty reduction in F_z as possible, so an accurate determination of the squeezing produced by a given experiment is of interest. However, such an absolute calibration of conditional spin-squeezing has not yet been achieved for a number of reasons. From a theory perspective, a quantitative model of the atom-probe scattering physics—the mechanism by which the measurement operates—has yet to be combined with a mathematically sound procedure for computing the degree of squeezing from that model. Experimentally, with one exception, laboratory data has not been amenable to the types of statistical analyses required for analyzing the squeezing in a well-controlled fashion as this is most reliably performed in the context of broadband quantum-limited detection [7, 8].

Specifically, the interpretation of existing squeezing experiments has (at least implicitly) assumed that polarimetric detection of the forward scattered probe laser yields a detector photocurrent [21],

$$y_t dt = \frac{P}{2M} F_z dt + dW_t. \quad (3)$$

In this expression, M is a constant of proportionality

known as the measurement strength that describes the rate at which photodetection provides information about F_z . The dW_t are quantum noises that result from vacuum fluctuations in the probe laser which exhibit Gaussian white statistics $\mathbb{E}[dW_t] = 0$ and $dW_t^2 = dt$ [25, 26, 27].

The measurement strength, M , is the most important parameter for determining the theoretical degree of squeezing that can be achieved as a result of the measurement. It is therefore important to determine M in terms of the properties of the atomic sample and probe laser such that experiment and theory can be compared. While the form of Eq. (3) has been derived in previous analyses [20, 21, 22, 23, 24], this was done by assuming that the atoms behave qualitatively like spin- $\frac{1}{2}$ particles.

However, spin-squeezing is generally performed using alkali atoms which exhibit higher spin [5, 7, 28], and recent experiments demonstrate that the deviation from spin- $\frac{1}{2}$ behavior can be significant [29]. While nonlinearities in the atom-probe scattering process are not always bad (proposals for capitalizing on these effects for quantum state tomography are being explored [30]), they raise serious complications for spin-squeezing experiments by invalidating the form of Eq. (3). Nonlinearities in the measurement interaction lead to additional atomic dephasing [29] and prevent the measurement from satisfying the most basic requirements of a quantum nondemolition interaction [1].

We find that the photocurrent in Eq. (3) can be recovered even for higher-spin atoms by suppressing tensor scattering interactions via a properly chosen experimental geometry. Using standard techniques [31, 32] to address the atom-probe scattering physics, combined with a semiclassical treatment of the atomic magnetization vector, we derive an expression for the measurement strength, M , in terms of characteristic experimental parameters. This allows us to obtain an expression for the photocurrent in terms of the duration of the measurement and the properties of the atomic system and the probe laser. We observe close agreement between our scattering model and data obtained using an apparatus of the type in Fig. 2.

By adopting a filtering treatment of the measurement photocurrent based on Bayesian conditioning, we derive an expression for the expected degree of spin-squeezing in terms of the signal-to-noise ratio of the measurement photocurrent. We also relate the signal to noise to the laboratory parameters that characterize the measurement in experiments of the form in Fig. 2. This allows us to develop a procedure for independently calibrating the degree of spin squeezing expected given the conditions under which our measurement data is acquired. The results we obtain are valid in the short-measurement limit in which atomic decoherence due to scattering probe light in unobserved (non-paraxial) electromagnetic modes [33] can be safely ignored. Current spin-squeezing experiments all fall into this regime where the degree of quantum uncertainty reduction is small compared to the Heisenberg spin-squeezing limit [2].

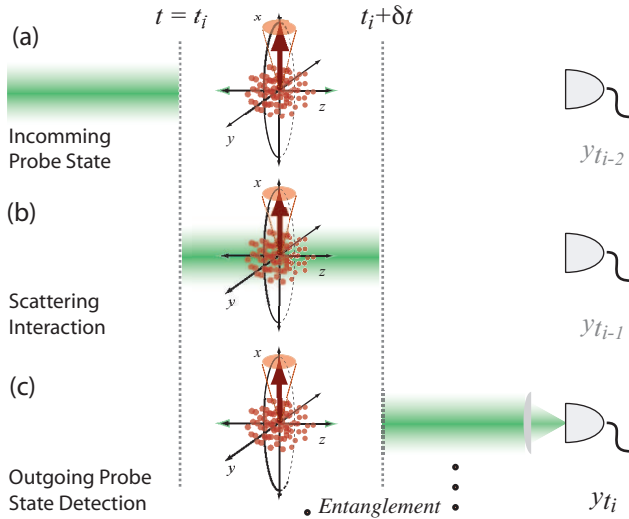


FIG. 3: (color online) The continuous measurement is treated by dividing the full measurement time into small slices during each of which the probe field interacts with the atomic system according to a scattering interaction that entangles the atoms and probe. Continuous photodetection of the forward-scattered probe field provides the measurement output.

II. CONTINUOUS MEASUREMENT AND THE ATOM-PROBE SCATTERING PROCESS

Our treatment of conditional spin-squeezing is accomplished by discretizing the continuous measurement, performed over the time period, $0 \leq t \leq T$, into slices of duration Δt . These slices are delimited by the points, $t_0, t_1, t_2, \dots, t_i, \dots, t_{i+1}, \dots, t_T$. We also decompose the probe field Hilbert space, \mathcal{H}_P , in a corresponding fashion,

$$\mathcal{H}_P = \mathcal{H}_P^{t_0} \otimes \mathcal{H}_P^{t_1} \otimes \mathcal{H}_P^{t_2} \otimes \dots \otimes \mathcal{H}_P^{t_{i+1}} \otimes \dots \otimes \mathcal{H}_P^{t_T}; \quad (4)$$

where the quantum state of the probe field during the i^{th} measurement time slice is described by the reduced density operator, $\hat{\rho}_{t_i}(t) \in \mathcal{H}_P^{t_i}$. Essentially, this is a decomposition of the probe field into temporal modes indexed by their associated time-slice, $t_i \leq t < t_{i+1}$ [24].

We can visualize each slice of the measurement as a scattering interaction between the probe field and the atoms followed by detection of the probe. In the Schrödinger picture, it is convenient to adopt the (not-too-inaccurate) cartoon in Fig. 3. At time, $t < t_i$ [Fig. 3(a)], the mode of the probe field corresponding to the i^{th} time-slice approaches the atomic spin system but has not yet interacted with it. Therefore at $t = t_i$, the joint quantum state for the atoms and the approaching field mode is separable,

$$\hat{\rho}(t_i) = \hat{\rho}(t_i) \otimes \hat{\rho}_i(t_i); \quad (5)$$

Here, $\hat{\rho}_i(t_i) \in \mathcal{H}_A^{t_i}$ is the reduced atomic density operator and $\hat{\rho}(t) \in \mathcal{H}_A^{t_i} \otimes \mathcal{H}_P^{t_i}$ is the full density operator for the joint system during the i^{th} time-slice (it reflects the full

history of the atomic system's evolution). The scattering interaction [Fig. 3(b)] is treated (in the Schrödinger picture) by propagating the state of the joint atom-probe system from t_i to $t_i + \Delta t$,

$$\hat{\rho}(t_i + \Delta t) = \hat{U}_t \hat{\rho}(t_i) \hat{U}_t^\dagger(t_i) \hat{U}_t^\dagger(t_i) \hat{U}_t^y(t_i); \quad (6)$$

using the time-evolution operator,

$$\hat{U}_t = \exp \left(-\frac{i}{\hbar} \hat{H}_s t \right); \quad (7)$$

for the Hamiltonian, \hat{H}_s , that governs the scattering interaction. Entanglement between the atoms and probe field is generated as a result of the coupling induced by the interaction Hamiltonian, \hat{H}_s .

This coupling ceases at $t_i + \Delta t$ and the outgoing probe is detected [Fig. 3(c)]. It is most convenient to treat this detection process in the Heisenberg picture where the quantum state is time-independent, $\hat{\rho}(t + \Delta t) = \hat{\rho}(t)$, but the operator describing the measurement evolves,

$$Y_{t+\Delta t} = \hat{U}_t^y \hat{U}_t^y \hat{\mathbb{1}}_A \hat{\rho}_t \hat{U}_t \hat{U}_t^\dagger \quad (8)$$

where $\hat{\mathbb{1}}_A$ is the identity operator on the atomic Hilbert space (the atoms are indirectly observed), $\hat{\rho}_t$ is the Heisenberg picture operator for the probe field observable measured by the detector and \hat{U}_t is the evolution operator from time zero to t .

Our approach will be to approximate the continuous measurement by taking Δt to be the time required for probe light to traverse the atomic sample. This duration is generally quite small compared to all other experimental time-scales, so it provides a realistic approximation of a true continuous measurement where $\Delta t \ll 0$. As such, we will refer to y_t as the continuous photocurrent. A mathematically rigorous treatment of the $\Delta t \ll 0$ limit would be provided by taking the quantum Markov limit [27, 34] derived using the Van Hove procedure [35], where the scattering Hamiltonian, $\hat{H}_s = \hat{H}_s(t)$, is parameterized by a weak-coupling parameter, κ , and time is rescaled, $t \rightarrow \kappa t$, as $\Delta t \rightarrow 0$. Our coarse-grained approach nonetheless provides a model that is both intuitive and agrees well with experiment.

A. Scattering Hamiltonian

To proceed, we must obtain an expression for the time-evolution operator, \hat{U}_t , by addressing the interaction between the atoms and the probe field. The scattering process described above can be described by first considering a Hamiltonian [17, 32, 36] that describes the interaction of a single atom with the probe field (a detailed discussion is provided in the Appendix),

$$\hat{H} = \hat{E}^{(+)}(\mathbf{r}; t) \frac{\partial \hat{d}^y}{\partial \mathbf{r}} \hat{E}^{(+)}(\mathbf{r}; t); \quad (9)$$

where \hat{d}^y and \hat{d} are the vector dipole atom ic raising and lowering operators and δ is the probe detuning from the relevant atom ic transitions. The negative and positive frequency eld operators, $\hat{E}^{(-)}$ and $\hat{E}^{(+)}$, describe the creation and annihilation of photons in the contributing probe modes. This Ham iltonian has a satisfying physical interpretation as a scattering interaction: the atom is first brought from its ground state to a virtual excited state via the raising operator, \hat{d}^y , by annihilating a photon from the probe eld through $\hat{E}^{(+)}$. Then, the temporarily excited atom returns to a (potentially different) ground state by emitting a photon into a (potentially different) scattered probe mode via \hat{d} and $\hat{E}^{(-)}$.

The central operator in the scattering Ham iltonian,

$$\hat{\Lambda} = \hat{d}\hat{d}^y; \quad (10)$$

commonly called the atom ic polarizability tensor, is a dyad involving vector operators [31]. Thus $\hat{\Lambda}$ is a rank-2 spherical tensor that can be decomposed into irreducible components,

$$\hat{\Lambda} = \hat{\Lambda}^{(0)} + \hat{\Lambda}^{(1)} + \hat{\Lambda}^{(2)}; \quad (11)$$

The scattering Ham iltonian similarly decomposes into irreducible spherical tensor operators,

$$\hat{H} = \hat{H}^{(0)} + \hat{H}^{(1)} + \hat{H}^{(2)} \quad (12)$$

where $\hat{H}^{(0)}$ is a scalar contribution, $\hat{H}^{(1)}$ transforms as a vector, and $\hat{H}^{(2)}$ transforms as a rank-2 symmetric tensor in the group representation theory of $SO(3)$. Were the atom ic system composed of spin- $\frac{1}{2}$ particles, it would be possible to neglect the rank-2 Ham iltonian [32], however, we can not do so for higher-spin Alkali atoms [28, 29, 37].

The full Ham iltonian for the collective atom ic spin resulting from N atoms is obtained by taking the symmetric sum of these single particle operators,

$$\hat{H}_N = \sum_{i=1}^N \hat{H}_i; \quad (13)$$

where $\hat{H}_i = \hat{1}_{i-1} \hat{H} \hat{1}_{i+1}$ is the single particle Ham iltonian acting on the i^{th} atom in the sample.

1. Scattering a Linearly Polarized Probe Field

Although the input probe state is linearly polarized, we must allow for the possibility of an arbitrarily polarized scattered state. In general, this implies that we must consider outgoing eld modes over all possible wavevectors and polarizations, but it is possible to restrict the analysis to only two paraxial modes (with orthogonal polarization vectors) if the polarimeter photodetectors (refer to the schematic in Fig. 2) image most of a small solid angle in the forward scattering direction. Neglecting non-paraxial modes prevents us from computing the

decoherence rate of the atom ic magnetization, but it does not limit our ability to analyze the spin-squeezing in the small-decoherence (short measurement time) limit.

The restriction to paraxial modes prevents us to consider eld operators,

$$\hat{E}_t^{(-)} = \frac{p}{\sim g} \frac{h}{\hat{a}^y_{\text{,}t} e^- + \hat{a}_{+,\text{t}}^y e^+} \hat{1}_i \quad (14)$$

and

$$\hat{E}_t^{(+)} = \frac{p}{\sim g} \frac{h}{\hat{a}_{\text{,}t} e^- + \hat{a}_{+,\text{t}}^y e^+} \hat{1}_i \quad (15)$$

where $\hat{a}^y_{\text{,}t}$ and $\hat{a}_{\text{,}t}$ are Heisenberg-picture creation and annihilation operators for the z -axis propagating mode with left circular polarization and $\hat{a}_{+,\text{t}}^y$ and $\hat{a}_{+,\text{t}}$ are the creation and annihilation operators for right circular polarization. The coefficient, $g = 1_0 = (2 \text{ eV})$, is a form factor, and e^- and e^+ are the (complex) spherical basis vectors for left and right helicity.

The Scalar Ham iltonian. The single-particle scalar scattering Ham iltonian, ${}^{(i)}\hat{H}^{(0)}$ (we will often drop the (i) superscript to avoid clutter when doing so is not ambiguous), can be represented as a product of operators on the separate atom ic and probe eld Hilbert spaces. This is accomplished by combining the expressions for the eld mode operators, Eqs. (14) and (15), with the rank-0 irreducible component of the atom ic polarizability tensor,

$${}^{(i)}\hat{H}^{(0)} = \hat{E}_t^{(-)} \frac{\hat{\Lambda}^{(0)}}{\sim} \hat{E}_t^{(+)}; \quad (16)$$

Evaluating this Ham iltonian using the form of the rank-0 atom ic polarizability derived in the Appendix leads to the scalar scattering Ham iltonian,

$$\begin{aligned} \hat{H}^{(0)} &= \frac{X}{\sim g} \frac{\frac{(0)}{f;f^0} h}{\frac{f;f^0}{f;f^0}} \hat{a}^y_{\text{,}t} \hat{a}_{\text{,}t} + \hat{a}_{+,\text{t}}^y \hat{a}_{+,\text{t}} \hat{1}_f \\ &= \frac{X}{\sim g} \frac{\frac{(0)}{f;f^0}}{\frac{f;f^0}{f;f^0}} \hat{S}_{0,\text{t}} \hat{1}_f; \end{aligned} \quad (17)$$

There are a number of terms in this expression: V is the scattering interaction volume, f is the spin quantum number of the ground atom ic hyperfine state, and f^0 labels all relevant excited states coupled by the probe eld. We have also defined the probe detuning, $\delta_{f,f^0} = \omega_{f,f^0} - \omega_f$, with respect to hyperfine transitions between f and f^0 , and the constants ω_0 and ω_{f,f^0} are related to the transition dipole matrix elements for the atom ic hyperfine transitions. These terms are derived in the Appendix [refer to Eqs. (A 10) and (A 17)]. The operator, $\hat{1}_f$ is the identity acting on the atom ic Hilbert space and $\hat{S}_{0,\text{t}}$ is the Schwinger boson operator,

$$\hat{S}_{0,\text{t}} = \frac{1}{2} \hat{a}_{+,\text{t}}^y \hat{a}_{+,\text{t}} + \hat{a}_{+,\text{t}}^y \hat{a}_{\text{,}t}; \quad (18)$$

for the probe field. Evidently, the rank-0 Hamiltonian couples the atomic identity operator to the field mode number operators and can be interpreted as an atomic state-independent light shift. It therefore affects both polarization modes of the probe field in an equivalent manner and will not contribute to the measurement since it does not provide any state-dependent information.

The Vector Hamiltonian. The vector contribution to the atom-probe scattering Hamiltonian,

$${}^{(1)}\hat{H}^{(1)} = \hat{E}_t^{(+)} \underbrace{\hat{E}_t^{(+)}}_{\sim} \hat{E}_t^{(+)}; \quad (19)$$

can be evaluated in a similar manner using expressions for the rank-1 polarizability derived in the Appendix,

$$\begin{aligned} \hat{H}^{(1)} &= {}_0g \frac{X}{f^0} \frac{\frac{(1)}{f;f^0} h}{\frac{(1)}{f;f^0}} \hat{a}_{+;t}^y \hat{a}_{+;t}^i \hat{a}_{+;t}^y \hat{a}_{+;t}^i \hat{f}_z \\ &= {}_0g \frac{X}{f^0} \frac{\frac{(1)}{f;f^0}}{\frac{(1)}{f;f^0}} \hat{S}_{z;t} \hat{f}_z : \end{aligned} \quad (20)$$

Here, the vector polarizability constant, $\frac{(1)}{f;f^0}$, is given by Eq. (A 21), \hat{f}_z is the z-component of the (single-particle) atomic spin angular momentum and $\hat{S}_{z;t}$ is the Schrödinger boson operator,

$$\hat{S}_{z;t} = \frac{1}{2} \hat{a}_{+;t}^y \hat{a}_{+;t}^i \hat{a}_{+;t}^y \hat{a}_{+;t}^i : \quad (21)$$

The rank-1 Hamiltonian can be interpreted as causing a differential phase shift on the two circular polarization modes by an amount that is proportional to the z-component of the atomic angular momentum. That is, the vector Hamiltonian leads to optical activity in the atomic sample and produces the familiar Faraday rotation effect often used to address continuous measurement of collective spin [18, 20, 22, 23, 24].

The Tensor Hamiltonian. Finally the tensor Hamiltonian,

$${}^{(1)}\hat{H}^{(2)} = \hat{E}_t^{(+)} \underbrace{\hat{E}_t^{(+)}}_{\sim} \hat{E}_t^{(+)}; \quad (22)$$

can be evaluated using expressions for the rank-2 polarizability derived in the Appendix to give,

$$\begin{aligned} \hat{H}^{(2)} &= {}_0g \frac{X}{f^0} \frac{\frac{(2)}{f;f^0}}{2 \frac{(2)}{f;f^0}} \hat{a}_{+;t}^y \hat{a}_{+;t}^i \hat{f}_+^2 + \hat{a}_{+;t}^y \hat{a}_{+;t}^i \hat{f}_-^2 \\ &+ 2 \hat{a}_{+;t}^y \hat{a}_{+;t}^i + \hat{a}_{+;t}^y \hat{a}_{+;t}^i 3\hat{f}_z^2 f(f+1)\hat{1}_f \\ &= {}_0g \frac{X}{f^0} \frac{\frac{(2)}{f;f^0}}{\frac{(2)}{f;f^0}} \hat{S}_{x;t} \hat{f}_x^2 \hat{f}_y^2 \\ &\hat{S}_{y;t} \hat{f}_x^2 \hat{f}_y^2 + \hat{f}_y^2 \hat{f}_x^2 \\ &+ \frac{2\hat{S}_{0;t}}{6} 3\hat{f}_z^2 f(f+1)\hat{1}_f : \end{aligned} \quad (23)$$

Here, the tensor polarizability constant, $\frac{(2)}{f;f^0}$, is given by Eq. (A 26) and $\hat{S}_{x;t}$ and $\hat{S}_{y;t}$ are the Schrödinger boson operators,

$$\begin{aligned} \hat{S}_{x;t} &= \frac{1}{2} \hat{a}_{+;t}^y \hat{a}_{+;t}^i + \hat{a}_{+;t}^y \hat{a}_{+;t}^i \hat{a}_{+;t}^y \hat{a}_{+;t}^i \hat{f}_z \\ \hat{S}_{y;t} &= \frac{1}{2} \hat{a}_{+;t}^y \hat{a}_{+;t}^i \hat{a}_{+;t}^y \hat{a}_{+;t}^i : \end{aligned} \quad (24)$$

The rank-2 Hamiltonian couples spin coordinates to the elliptical components of the probe laser field and produces a second-order light shift proportional to the atomic quadrupole moment. These terms, which only arise for particles with spin greater than 1/2, lead to an elliptically polarized scattered probe field [28, 31]. The rank-2 interaction potentially limits the validity of any analysis of a continuous measurement of collective atomic spin in alkali atoms based on the qualitative behavior of spin-1/2 particles. Fortunately, as demonstrated below, it is possible to identify experimental conditions that dramatically suppress the tensor interaction.

B. Time Evolution Operator

With the polarizability Hamiltonian decomposed into its irreducible spherical tensor representation, we are now in a position to derive an expression for the time evolution operator, \hat{U}_t , defined in Eq. (7). This amounts to evaluating \hat{U}_t using $\hat{H}_N = \hat{H}_N^{(0)} + \hat{H}_N^{(1)} + \hat{H}_N^{(2)}$.

1. Semiclassical Approximation

In the spirit of treating the atomic sample as a large, classical magnetization vector with transverse quantum uncertainty, it is appropriate to invoke a semiclassical treatment of the atom-probe scattering interaction. That is, we approximate the Hamiltonian, \hat{H}_N , by replacing symmetric sums over single-particle atomic spin operators with the component of the classical magnetization vector associated with that atomic operator,

$$\begin{aligned} &X \quad {}^{(1)}\hat{f}_x \quad ! \quad F_x = N f \sin \theta \cos \phi \\ &\quad i=1 \\ &X \quad {}^{(1)}\hat{f}_y \quad ! \quad F_y = N f \sin \theta \sin \phi \\ &\quad i=1 \\ &X \quad {}^{(1)}\hat{f}_z \quad ! \quad F_z = N f \cos \theta ; \\ &\quad i=1 \end{aligned} \quad (25)$$

etc. We have also transformed F into spherical coordinates where the angles, θ and ϕ , are defined with respect to the laboratory coordinate system in Fig. 4.

Within the semiclassical approximation, we obtain an effective scattering interaction Hamiltonian, $\hat{H}' = \hat{H}_N^{(0)} +$

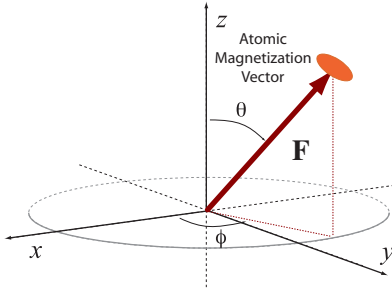


FIG. 4: (color online) Definition of the spherical coordinate angles used to describe the orientation of the collective atomic magnetization vector, \mathbf{F} , relative to the fixed laboratory cartesian coordinate system. The polarization vector of the input probe light resides in the xy -plane and forms an angle, ϕ , with respect to the laboratory x -axis.

$H_N^{(1)} + H_N^{(2)}$ that only involves operators on the probe field Hilbert space. However, it is possible to further simplify the resulting expressions by recognizing that photodetection cannot detect changes in the overall phase of the scattered probe field (i.e., phases common to both circular polarization modes). We can neglect all terms in the semiclassical Hamiltonian involving $\hat{S}_{0,\tau}$, including the entire scalar interaction and the rank-2 light shift. The resulting effective scattering interaction assumes the final form, $H = H_N^{(1)} + H_N^{(2)}$, where

$$H_N^{(1)} = N f_0 g \frac{\mathbf{X}}{f^0} \frac{(1)}{f;f^0} \cos \hat{S}_{z,\tau} \quad (26)$$

$$H_N^{(2)} = N f^2 g \frac{\mathbf{X}}{f^0} \frac{(2)}{f;f^0} \quad (27)$$

$$\sin \cos' \hat{S}_{x,\tau} \quad \sin \sin' \hat{S}_{y,\tau} :$$

We demonstrate in Sec. IV that this semiclassical approximation leads to a model that agrees strongly with experimental data.

2. Semiclassical Time-Evolution Operator

We now have all the necessary expressions to evaluate the time-evolution operator, U_t under the semiclassical approximation. Recognizing that we must account for the action of the output half-wave plate used to balance the polarimeter (refer to Fig. 2) which enacts a $\pi/2$ z -axis rotation of the probe Stokes vector,

$$U_{-2} = \exp \frac{\hbar}{2} \hat{S}_{z,\tau} ; \quad (28)$$

we arrive at the time-evolution operator,

$$U_t = \hat{U}_{-2} \exp \frac{\hbar}{2} i (\hat{S}_{x,\tau} + \hat{S}_{y,\tau} + \hat{S}_{z,\tau}) : \quad (29)$$

The rotation angles are given by,

$$x = \frac{1}{2} \frac{\omega_0 f^2 \sin \theta \cos' \mathbf{X}}{f^0} \frac{(2)}{f;f^0} \quad (30)$$

$$y = \frac{1}{2} \frac{\omega_0 f^2 \sin \theta \sin' \mathbf{X}}{f^0} \frac{(2)}{f;f^0} \quad (31)$$

$$z = \frac{\omega_0 f \cos \theta}{f^0} \frac{\mathbf{X}}{f;f^0} \frac{(1)}{f;f^0} \quad (32)$$

and all involve an orientation-independent coupling parameter, ω_0 , that contains rank-independent atomic polarizability factors,

$$\omega_0 = N \frac{3}{4} \frac{\omega_0^2}{r^2} : \quad (33)$$

Here, ω_0 is the atomic spontaneous emission rate, ω_0 is the atomic transition wavelength, N , is the number of atoms, and r is the atom cloud radius. In obtaining these interaction parameters we have used the interaction time,

$$t = \frac{4r}{3c} \quad (34)$$

corresponding to the transit time of probe light through the atomic sample and the field coefficient,

$$g = \frac{\omega_0}{2 \omega_0 V} = \frac{3 \omega_0}{8 \omega_0 r^3} ; \quad (35)$$

where ω_0 is the atomic resonance frequency and V is the interaction volume (the volume of the atomic sample).

From an experimental standpoint, it is useful to note that ω_0 is directly related to the on-resonance optical depth of the atomic sample (which is sometimes more easily characterized than the atom number and trap volume),

$$\omega_0 = \frac{N \omega_0}{2A} = \frac{\Omega D}{2} ; \quad (36)$$

where $\omega_0 = 3 \frac{\omega_0^2}{r^2} = 2$ is the resonant atomic scattering cross section and $A = \pi r^2$ is the cross-sectional area of the atomic sample.

C. The Polarimeter Photocurrent

We are finally in a position to compute the time-evolved Heisenberg-picture detection operator, \hat{U}_t that appears in Eq. (8). For a balanced polarimeter that measures the polarization between horizontal and vertical linear polarizations, the detectors implement a measurement of $\hat{S}_{x,\tau} = \hat{S}_{x,\tau}$. This leads to the photocurrent,

$$\begin{aligned} Y_t^{(x)} &= \hat{U}_t^y \hat{U}_t^y \hat{S}_{x,\tau} \hat{U}_t^y \hat{U}_t^y = \hat{U}_t^y \hat{S}_{x,\tau} \hat{U}_t^y \\ &= \frac{x}{2} \frac{y}{2} (1 - \cos \phi) - \frac{z}{2} \sin \phi + (\hat{E}_t^{(+)} + \hat{E}_t^{(-)}) ; \end{aligned} \quad (37)$$

where we made use of the fact that U_t and U_{-t} commute and we have defined the angle,

$$= \frac{q}{\sqrt{x^2 + y^2 + z^2}}: \quad (38)$$

The superscript (x) on the photocurrent denotes the fact that we are measuring $\hat{S}_{x,t}$.

Note the appearance of the free input field, $\hat{E}_t^{(+)} + \hat{E}_t^{(-)}$, in Eq. (37). Evidently, the photocurrent decomposes into the sum of this input field and source terms involving the atomic degrees of freedom. We will identify the free-field as quantum noise, not surprisingly, since the photocurrent is obtained from a continuous sequence of independent measurements on the scattered probe; each of these exhibits randomness due to optical shotnoise.

It is also possible to evaluate the other time-evolved probe field Schwinger boson operators as these are physical observables that correspond simply to operating the polarimeter in different bases. For a measurement of $\hat{S}_{y,t}$ we obtain,

$$\begin{aligned} Y_t^{(y)} &= U_t^y \hat{S}_{y,t} U_{-t} \\ &= \frac{x^2}{2^2} + \frac{y^2 + z^2}{2^2} \cos(\theta) + \hat{E}_t^{(+)} + \hat{E}_t^{(-)}; \end{aligned} \quad (39)$$

and for $\hat{S}_{z,t}$,

$$\begin{aligned} Y_t^{(z)} &= U_t^y \hat{S}_{z,t} U_{-t} \\ &= \frac{y}{2} \sin(\theta) + \frac{x z}{2^2} (1 - \cos(\theta)) + \hat{E}_t^{(+)} + \hat{E}_t^{(-)}; \end{aligned} \quad (40)$$

These expressions were all obtained by employing the Cramér-Baker-Hausdorff procedure.

D. Spin-Squeezing Measurements

Returning to the balanced polarimeter photocurrent in Eq. (37), our goal is to find conditions where the measurement assumes (at least nearly) the ideal form in Eq. (8) as this will allow us to generate spin-squeezing. It is readily shown that all terms not linear in F_z vanish in Eq. (37) provided that $\alpha = -2$ and $\beta = 0$. That is, a pure Faraday rotation Hamiltonian is recovered when the atomic magnetization vector is oriented along the x -axis. However, rotating F in the xy -plane results in elliptically polarized scattered probe light, and moving out of this plane results in nonlinear atomic dephasing due to scattering terms which are quadratic in the single-particle spin operators, $\langle \hat{f}_z \rangle$. These adverse effects are only avoided for the experimental geometry where F is collinear with the x -axis. Fortunately, spin-squeezing experiments are easily operated under such conditions [7].

Taking the input probe field to be in an x -polarized optical coherent state [38],

$$\hat{E}^{\dagger}(t) = j \hat{a}^{\dagger} h j - j h \hat{a} \quad (41)$$

with complex amplitude, j , in each paraxial polarization mode leads to the photocurrent,

$$Y_t = \frac{3N_f P}{4^2 r^2} \frac{x}{f^0} \frac{\frac{(1)}{f;f^0}}{\frac{(1)}{f;f^0}} \frac{1}{2} + t: \quad (42)$$

the optical probe power, P , is determined by the coherent state amplitude, $P = 2\sqrt{j^2}$. We have also relabeled the input field operator, $\hat{E}_t^{(+)} + \hat{E}_t^{(-)}$, as t to indicate that it represents measurement noise.

Closer inspection of Eq. (42) reveals that it is possible to reexpress the photocurrent in the form,

$$Y_t = \frac{P}{S F_z} + t: \quad (43)$$

where we call the constant, S , the scattering strength,

$$S = \frac{1}{\sim^2} \frac{3}{4} \frac{\frac{2P}{f^0}}{4^2 r^2} \frac{x}{f^0} \frac{\frac{(1)}{f;f^0}}{\frac{(1)}{f;f^0}} 5: \quad (44)$$

It has units of $W^2 = \text{Hz}^2$ (power squared per \sim^2) and characterizes the degree of coupling between the atoms and the probe field such that S quantifies the polarimeter optical power in balance per unit spin.

To arrive at an expression for the measurement strength, M as defined in Eq. (8), we must consider the variance, σ^2 , of the white noise increments t . For an optical coherent state [38, 39], doing so leads to the familiar shotnoise expression,

$$\sigma^2 = \mathbb{E}[t^2] = \frac{1}{2} \sim^2 P; \quad (45)$$

which has units of $W^2 = \text{Hz}$ (power squared per frequency). The measurement strength is given by the ratio,

$$M = \frac{\sim^2 S}{2}; \quad (46)$$

which has units of Hz (frequency) as expected for a measurement of the rate at which the measurement reveals information about F_z [21, 22, 23, 24, 40]. Our expression is similar to previous derivations [21, 24, 41] in that it appears as a Faraday rotation signal. However, our specific expressions for x , y and z account for the detailed hyperfine structure of the atomic excited states, including the fact that the oscillator strengths and signs of the contributions from different participating excited states are not equal, and doing so is required for quantitative agreement between theory and experiment.

Finally we note that the product of the scaled measurement strength, $M F$, and the duration, \sim , of the measurement,

$$\text{SNR} = \frac{P}{M F} \frac{S}{2} = \sim \frac{F S}{2}; \quad (47)$$

is a dimensionless parameter that should be interpreted as the signal-to-noise ratio of the measurement.

III. THE DEGREE OF CONDITIONAL SPIN-SQUEEZING

Equation (43) shows us that SF_z and the white noises, η_t , commute, so basic quantum mechanics takes over: a given measurement trajectory can be thought of as sampling a fixed classical F_z outcome from a distribution, $p_0(F_z)$, established by the initial quantum state of the spin system. Likewise, but at each point in time, the noises, η_t , are sampled from a distribution with Gaussian white statistics. Since these two aspects of the measurement commute, they are independent and the photocurrent assumes the form of an offset, SF_z , proportional to the z-component of the atomic magnetization, plus white noise. The problem of discerning F_z from the noisy measurement record therefore reduces to a filtering problem.

The physical interpretation of the scattering strength, S , is that in the absence of appreciable atomic decay or magnetic fields, it relates the z-component spin angular momentum to the photocurrent that would be measured were it possible to eliminate the white noise by perfect averaging,

$$y = \lim_{T \rightarrow 1} \frac{1}{T} \int_0^T y_t dt = \frac{p}{S} F_z; \quad (48)$$

Of course, given a real laboratory photocurrent, it is impossible to remove the quantum noise completely because the measurement record lasts a finite duration. Limiting the averaging period to this finite time yields a measurement,

$$y_{(0,1)} = \frac{1}{T} \int_0^T y_t dt = \frac{p}{S} F_z + \eta_{(0,1)}; \quad (49)$$

that still contains a random increment, $\eta_{(0,1)}$, albeit reduced. This residual stochastic term reflects quantum noise that survives the incomplete averaging period, $0 < t < T$, and its statistics are also Gaussian,

$$p(\eta_{(0,1)}) = \frac{1}{2\pi} \exp\left(-\frac{\eta_{(0,1)}^2}{2}\right); \quad (50)$$

where,

$$\mathbb{E}[\eta_{(0,1)}^2] = \frac{1}{2}; \quad (51)$$

The variance of the iterated noise, η^2 , decreases inversely with the measurement duration as expected since longer averaging better suppresses the white noise.

These concepts are illustrated by the simulated measurement trajectory in Fig. 5. The plot begins with the probe laser turned off, during which all necessary state preparation of the atomic system such as atom trapping, cooling and optical pumping into an x-polarized coherent spin state is performed. Once the probe light is enabled at $t = 0$, the photocurrent acquires a mean offset, SF_z , proportional to the spin measurement outcome, F_z , but

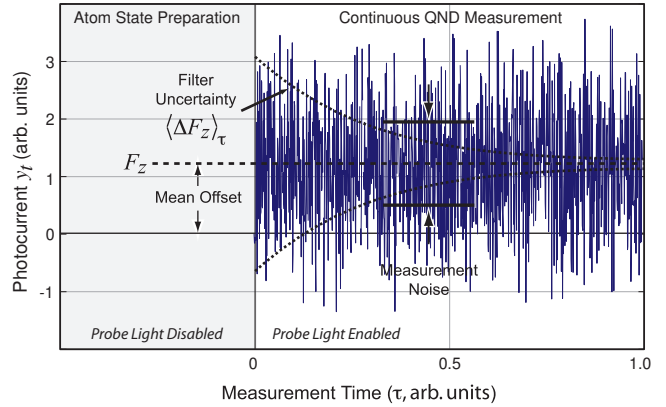


FIG. 5: (color online) Simulated photocurrent for a continuous measurement of atomic spin angular momentum via balanced polarimetry. At the onset of the measurement, $t = 0$, the photocurrent assumes a mean offset proportional to the z-component of the spin, but this offset is masked by white noise due, in part, to optical shotnoise on the probe laser. Filtering the photocurrent gradually reduces the uncertainty in the photocurrent offset and produces spin-squeezing.

this mean value is masked by photocurrent noise. At short times, the signal is overwhelmed by local statistical fluctuations; however, averaging the photocurrent suppresses the uncertainty in the mean signal by integrating away the white noise, illustrated by the dotted lines in Fig. 5.

Reduced uncertainty in the mean polarimeter signal obtained by filtering the photocurrent corresponds directly to reduced uncertainty in F_z with respect to its initial coherent state variance; this is conditional spin-squeezing [7, 13, 42]. Furthermore, the amount of quantum state reduction is determined by how well the z-component of the atomic spin angular momentum can be resolved from the polarimeter photocurrent in the presence of photocurrent noise.

A. Filtering and the Degree of Squeezing

For a coherent spin state polarized along the x-axis, $\hat{F}(0) = \hat{F}_x \hat{F}_y$, the measurement-outcome distribution is very nearly Gaussian [13, 21],

$$p_0(F_z) = \frac{1}{\sqrt{2\pi}} \exp\left(-\frac{F_z^2}{2}\right); \quad (52)$$

with mean,

$$\hat{F}_z i = \int_1^{Z+1} F_z p_0(F_z) dF_z = 0; \quad (53)$$

and variance,

$$\hat{F}_z^2 i = \int_1^{Z+1} (F_z - \hat{F}_z i)^2 p_0(F_z) dF_z = \frac{1}{2} F_z^2; \quad (54)$$

equal to the coherent state spin projection noise [12]. From a filtering and estimation perspective, hF_{zi} and hF_z^2i describe our prior knowledge of the measurement outcome e , in terms of the net atom magnetization, $\sim F$. Quantum mechanically, this probability distribution has the interpretation that the classical outcome e , F_z , will be obtained with probability $p_0(F_z)$ in a statistical ensemble of F_z measurements performed on a large collection of similarly prepared coherent spin states.

1. Bayesian Conditional Updating

Once the measurement process begins, the prior distribution $p_0(F_z)$ must be updated to remain consistent with the information gained from the photocurrent acquired over the interval $0 < t < \tau$. That is, we must determine the conditional probability, $p(F_z | y_{[0, \tau]})$, of the measurement outcome e , F_z , given the average photocurrent, $y_{[0, \tau]}$. This is accomplished by employing Bayes' rule,

$$p(F_z | y_{[0, \tau]}) = \frac{p(y_{[0, \tau]} | F_z) p_0(F_z)}{p(y_{[0, \tau]})} : \quad (55)$$

Here, $p(y_{[0, \tau]} | F_z)$ is the probability of observing the average photocurrent, $y_{[0, \tau]}$, given that the measurement outcome e is F_z , and $p(y_{[0, \tau]})$ is the unconditional probability of observing the photocurrent average $y_{[0, \tau]}$.

In order to utilize Eq. (55), it is necessary to obtain expressions for $p(y_{[0, \tau]} | F_z)$ and $p(y_{[0, \tau]})$, both of which implicitly involve the statistics of the residual Gaussian increment, $y_{[0, \tau]}$, in the average photocurrent. At this point, we recognize that the conditional distribution, $p(y_{[0, \tau]} | F_z)$, is given by the probability for observing the stochastic increment (filtered measurement innovation), $p_{[0, \tau]} = (y_{[0, \tau]} - SF_z)$,

$$p(y_{[0, \tau]} | F_z) = p(y_{[0, \tau]} - SF_z) : \quad (56)$$

Thus, the unconditional probability for the average photocurrent, $y_{[0, \tau]}$, can be readily computed by integrating Eq. (56) with respect to the prior distribution,

$$p(y_{[0, \tau]}) = \int p(y_{[0, \tau]} - SF_z) p(F_z) dF_z : \quad (57)$$

$$= \frac{1}{\sqrt{2\pi(SF_z^2 + 2^2)}} \exp\left(-\frac{y_{[0, \tau]}^2}{SF_z^2 + 2^2}\right) :$$

With Eqs. (56) and (57) in hand, it is now possible to evaluate the Bayesian update rule in Eq. (55),

$$p(F_z | y_{[0, \tau]}) = \frac{p(F_z) p(y_{[0, \tau]} | F_z) p_0(F_z)}{p(y_{[0, \tau]})} : \quad (58)$$

$$= \frac{2^{-\frac{F_z^2}{2} - \frac{SF_z^2}{2}}}{2^{-\frac{y_{[0, \tau]}^2}{2} - \frac{SF_z^2 + 2^2}{2}}} \exp\left(-\frac{(SF_z - y_{[0, \tau]})^2}{2^2(SF_z^2 + 2^2)}\right) :$$

The expectation value of the spin measurement outcome e , hF_{zi} , can be computed from the updated conditional probability,

$$hF_{zi} = \int F_z p(F_z | y_{[0, \tau]}) dF_z : \quad (59)$$

$$= \frac{p(SF_z^2 y_{[0, \tau]})}{SF_z^2 + 2^2} :$$

along with its reduced variance,

$$hF_z^2 i = \int (F_z - hF_{zi})^2 p(F_z | y_{[0, \tau]}) dF_z : \quad (60)$$

$$= \frac{SF_z^2}{SF_z^2 + 2^2} :$$

We quantify the degree of squeezing, W , as the fractional reduction in the variance of the measurement outcome e with respect to the coherent state variance,

$$W = \frac{2hF_z^2 i}{\sim^2 F} = \frac{1}{1 + M F} = \frac{1}{1 + SNR^2} : \quad (61)$$

where M and SNR are defined in Eqs. (46) and (47). This squeezing measure has the interpretation that when $SNR = 1$, the photocurrent will display a mean equal to p , the standard deviation of $y_{[0, \tau]}$, when F_z is equal to $\sqrt{F_z^2 + 2^2}$, the standard deviation of the spin coherent state fluctuations. It should be noted that a signal to noise ratio of $SNR = 1$ corresponds to 3 dB of spin-squeezing (in variance) as $W(1) = \frac{1}{2}$. Furthermore, some degree of squeezing is produced by any finite signal to noise ratio, provided that the initial spin state is in fact a minimum uncertainty state. W is approximately equal to the squeezing parameter, β , as it is usually defined [2] in the absence of any appreciable decay in the total atom magnetization.

IV. MEASUREMENT MODEL VALIDATION

We tested this model of the continuous F_z measurement against laboratory data collected from our ongoing conditional spin-squeezing experiment involving laser cooled Cs atoms and balanced polarimetric detection of a forward-scattered, off-resonant probe laser field.

A. Experimental Apparatus

Figure 6 provides a schematic of the major components of the experimental apparatus. Our single-particle alkali atom spin system is the $6^2S_{1/2}$ ($F=4$) ground state hyperfine manifold in ^{133}Cs with 4% of intrinsic angular momentum due to a combination of the $i=7/2$ nuclear spin and the $s=1/2$ spin of an unpaired $6s$ valence electron. We obtain cold atom samples from a 10^{-8} Torr background Cs vapor using standard laser

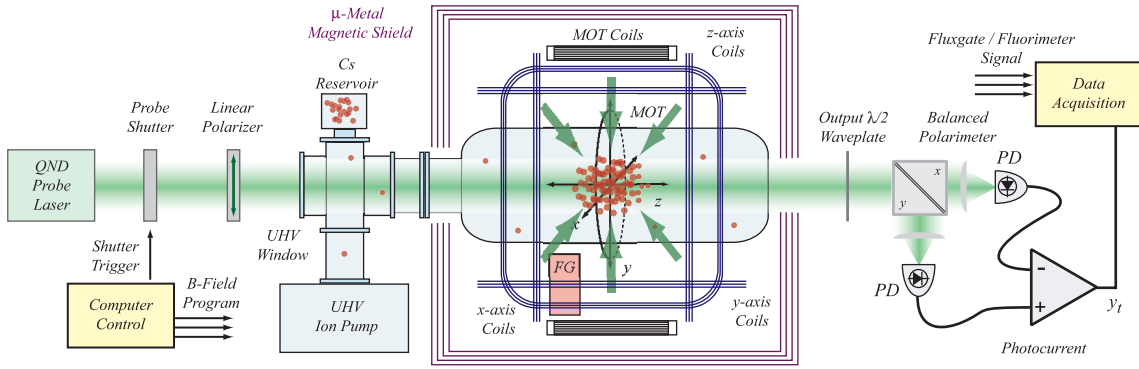


FIG. 6: (color online) Schematic of our experimental apparatus in which collective spin angular momentum of a cloud of laser cooled Cs atoms is measured by polarimetric detection of a scattered σ -resonant probe laser. Ambient magnetic field fluctuations are suppressed by magnetic shielding and can be monitored with a fluxgate magnetometer (FG) situated nearby the atomic sample. Components not shown include the optical pumping laser (aligned along the laboratory x -axis) and external trim coils used to zero ambient magnetic fields and their first order gradients.

cooling and trapping techniques by collecting between 10^9 and 10^{10} atoms in a magneto-optic trap (MOT) with a radiation-pressure limited density of $8 \cdot 10^0$ atoms / cm^3 . Trapping beams are derived from a 150 mW injection-locked diode laser tuned (11-15) MHz red of the Cs $6^2\text{S}_{1/2}$ ($F=4$)! $6^2\text{P}_{3/2}$ ($F=5$) cycling transition. Each 35 mW trapping beam has an approximately constant intensity profile and a 2.5 cm diameter. A 10 mW repump laser tuned to the $6^2\text{S}_{1/2}$ ($F=3$)! $6^2\text{P}_{3/2}$ ($F=4$) transition is used to prevent atomic population from decaying out of the trapping cycling transition.

Following the atom collection phase, the sample is sub-Doppler cooled [43] to a temperature of $T = 5$ K and the initial x -polarized spin state is prepared with a circularly polarized 100 W optical pumping beam (pulsed for 2-4 ms) propagating along the x -axis and tuned to the ($F=4$)! ($F=4$) hyperfine transition. A 100 mG magnetic holding field is applied along the laboratory x -axis to define the optical pumping direction.

Continuous measurement of F_z is implemented with a nearly quantum shotnoise-limited probe laser that can be detuned from the $6^2\text{S}_{1/2}$ ($F=4$)! $6^2\text{P}_{3/2}$ ($F=5$) Cs transition over a range $\Delta = 1.4$ GHz. The probe beam is linearly polarized by a high extinction Glan-Thomson prism prior to passing through the cold atom cloud, and the orientation of the linear polarization vector with respect to the laboratory coordinate system may be rotated via an input half-waveplate. The scattered probe field is detected with a polarimeter constructed from a Glan-Thomson polarizing beam splitter and a DC-balanced photodetector with > 1 MHz measurement bandwidth.

A computer controls the experiment timing and records the polarimeter output as well as diagnostic information including background magnetic field fluctuations (measured with a flux-gate magnetometer) and atom number (measured by fluorescence imaging). The computer enables/disables the measurement by controlling a shutter on the probe laser, constructed from a

switched acousto-optic modulator, with 100 ns resolution. Magnetic fields with magnitudes up to 0.5 G can be applied in arbitrary (time-dependent) directions by driving 3 pairs of computer-controlled Helmholtz coils, oriented along the laboratory x -, y -, and z -axes, with a bandwidth of 1 MHz.

Background magnetic field fluctuations are suppressed through a combination of passive metal shielding and active field cancellation via external trim coils. Each atom preparation (trapping, cooling and optical pumping) and measurement cycle is synchronized with respect to the 60-Hz building power lines to suppress the effects of induced magnetic fields. Slow magnetic drift due to natural and anthropogenic sources are cancelled by adjusting the external trim coils based on the output of the fluxgate magnetometer. Measurement trajectories in which the field fluctuations lie outside of a specified tolerance (due to infrequent events such as opening/closing doors, building elevator motion, etc.) are discarded based on the fluxgate magnetometer reading.

B. Verification of the Probe Scattering Model

Our model of the scattered probe polarization as a function of the orientation of the atomic magnetization vector was compared against experiment by observing the polarimeter photocurrent as the orientation of the atomic polarization was varied according to different specified paths in the laboratory coordinate system. This was accomplished as follows. An x -polarized cold atom sample was prepared according to the description above and an x -axis magnetic holding field of 100 mG was applied. At this point, the probe shutter was opened and the balanced polarimeter photocurrent was monitored while the orientation of the magnetic holding field was varied according to the specified path. The rate of change of the holding field orientation was chosen to be slow com-

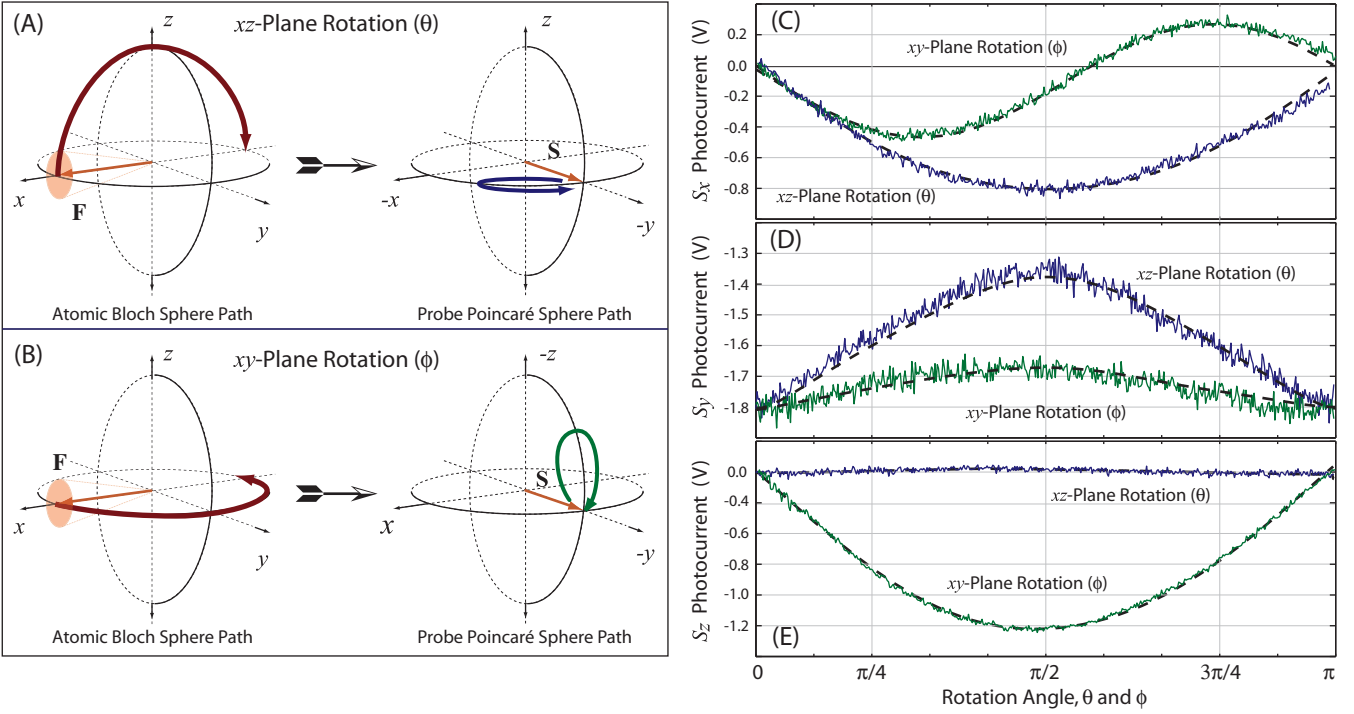


FIG. 7: (color online) Comparison of our model of continuous measurement with photocurrents obtained from our cold atom experiment with $N = 3 \times 10^9$ Cs atoms in an $r = 4$ mm spherical trap and a $P = 10$ W probe field blue-detuned from the $(F=4)$, $(F=5)$ D_2 hyperfine transition ($\lambda_0 = 852$ nm) by 150 MHz. The left panel illustrates the two adiabatic trajectories for the collective atomic spin and the corresponding polarization state of the scattered probe field. The right panel shows photocurrents obtained from polarimetric detection of the x - and z -components of the scattered probe Stokes vector as compared to theoretical predictions (dotted lines). All trajectory times are $\tau = 10$ ms, during which we observe negligible atomic decoherence. The difference in the scales of plots (C-E) reflect the different strengths of the vector and tensor interactions.

pared to the atomic Larmor precession frequency such that the atomic magnetization vector adiabatically followed the path traced by the holding field.

This process was performed for two different adiabatic paths on the atomic Bloch sphere, depicted in the left panel of Fig. 7 along with the corresponding scattered polarization state trajectories on the probe Poincaré sphere:

xz-Plane Rotation: the atomic magnetization follows a path beginning along the x -axis and rotates around the y -axis: $\theta = -2\pi/0$ with $\phi = 0$ followed by $\theta = 0\pi/2$ with $\phi = \pi/2$ [refer to Fig. 7(A)].

xy-Plane Rotation: the atomic magnetization follows a path beginning along the x -axis and rotates around the z -axis: $\theta = 0\pi/2$ with $\phi = -2\pi$ [refer to Fig. 7(B)].

We chose these two trajectories because they highlight the different contributions from the rank-1 and rank-2 scattering interactions. The xz-plane trajectory, where $\phi = 0$, virtually eliminates the rank-2 tensor contribution to the photocurrent leaving nearly ideal Faraday rotation while the xy-plane rotation produces elliptical scattered probe polarizations.

1. Measuring the Scattering Probe Stokes Vector

The right-hand panel of Fig. 7 compares the measured polarimeter photocurrents for these two adiabatic trajectories with those predicted by our atom-field scattering model (dotted curves). Fig. 7(C) reflects the x -component of the scattered Probe Stokes vector, measured by operating the polarimeter in balanced configuration (as is usually the case) to obtain a photocurrent, $y_{xt}^{(x)}$, of the form given in Eq. (37). Here we see the characteristic Faraday rotation signal produced by rotating the atomic magnetization in the xz-plane; the period of the Stokes vector precession is equal to that of the magnetization trajectory. The xy-plane trajectory produces a photocurrent that results from elliptically scattered probe light. This tensor scattering effect is characterized by a rotation period half that of the atomic magnetization, and the origin of this double-frequency feature is evident from the Stokes vector trajectory on the probe Poincaré sphere [Fig. 7(B)].

Fig. 7(D) reflects the y -component of the scattered Stokes vector measured by rotating the output waveplate by $\phi = \pi/4$. Operating the polarimeter in this (unbalanced) configuration enacts a measurement of $S_{yt}^{(y)}$ and yields a

photocurrent, $y_t^{(v)}$, with the form in Eq. (39). A gain we observe good agreement between the experimental and predicted (dotted curves) signals for both the rank-1 and rank-2 scattering interactions. As expected, the polarization state of the probe field is unaffected when the atom magnetization is parallel to the input optical polarization, i.e., oriented along the x -axis.

Finally, Fig. 7(E) was obtained by placing a $=4$ quarter-waveplate after the balancing output half-waveplate. In this configuration, the polarimeter operates in the circular basis and measures $\hat{S}_{z,t}$ to produce a photocurrent, $y_t^{(z)}$, of the form in Eq. (40). We see there is little elliptical character to the scattered probe polarization for the xz -plane trajectory. This observation is consistent with the predictions of our model (dotted lines) and reflects the fact that for $\gamma' = \gamma_p = 0$ the rank-2 interaction Hamiltonian vanishes. While nearly pure Faraday rotation occurs for the xz -plane rotation, significant elliptical polarizations are however observed for the xy -plane trajectory.

The predicted photocurrents plotted in Fig. 7 (dotted lines) were calculated using the characteristics of our polarimeter photodetector and the photocurrent expressions in Eqs. (37-40) according to the model,

$$y_t^{(\text{expt})} = gy_t^{(i)}; \quad (62)$$

where g is the transimpedance gain of the detector (in V/A) and i is the responsivity of the detector (in A/W). As such, we were able to generate the predicted photocurrents in Fig. 7 by evaluating Eqs. (37-40) using values for the atom number, trap volume, probe power and detuning consistent with independent characterizations of

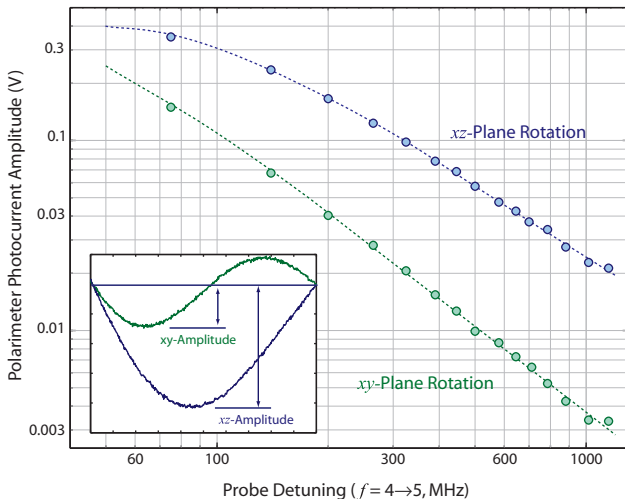


FIG. 8: (color online) Relative scaling of the rank-1 and rank-2 contributions to the photocurrent as a function of the probe detuning measured by the balanced polarimeter photocurrents for the two Bloch sphere trajectories defined in Fig. 7 (inset plot). Dotted lines indicate the scaling predicted by our probe scattering model.

those parameters. For our detector, $g = 3.62 \times 10^6 \text{ V/W}$. The atom number and trap volume were obtained from fluorescence detection of the MOT and a CCD image of the atom cloud, and the resulting values, $N = 3 \times 10^9$ and $r = 4 \text{ mm}$, correspond to an optical depth, OD = 16, which is consistent with absorption measurements that we performed. Given our uncertainty in measuring the number of atoms, it can be inferred that our optical pumping efficiency in these (relatively) optically thin atom samples is no less than 85% (but is more likely > 90%) [16].

Close agreement between predicted and observed photocurrents was only possible after including all excited hyperfine states in the CsD_2 transition and by accounting for their individual oscillator strengths. Deviations of the measured photocurrents relative to the predicted values seen in Fig. 7 are consistent with an input field that is not perfectly linearly polarized. This possibility is highly plausible considering that many of the optical elements, including the windows used to access the high-vacuum environment (refer to Fig. 6), exhibit some degree of birefringence, despite the fact that great care was taken to minimize any corruption of the input probe polarization.

2. Relative Scaling of the Scattering Terms with Probe Detuning

As a further verification of our scattering model, we investigated the scaling of the rank-1 and rank-2 contributions to the polarimeter photocurrent as a function of the probe detuning. As before, photocurrents were recorded for the xy -plane and xz -plane trajectories with the polarimeter operating in balanced configuration to measure the x -component of the probe Stokes vector. The magnitude of the vector and tensor scattering interactions were measured from the amplitude of the xz - and xy -plane rotations, respectively, as illustrated by the inset in Fig. 8. This plot compares these measured signal amplitudes with those predicted by our scattering model for detunings (with respect to the $(F=4)$) ($f=5$) hyperfine transition) ranging from 75 MHz to 1.1 GHz.

The fact that multiple excited state hyperfine levels participate in the scattering interaction is evident from scalings which are not constant in f^1 . As supported by our full model of the scattering interaction, we observe no qualitative difference in the continuous measurement for probe detunings smaller than the hyperfine splittings. This suggests that conditional spin-squeezing experiments can be performed with small detunings provided that the probe intensity is weak enough that the small decoherence requirement is satisfied.

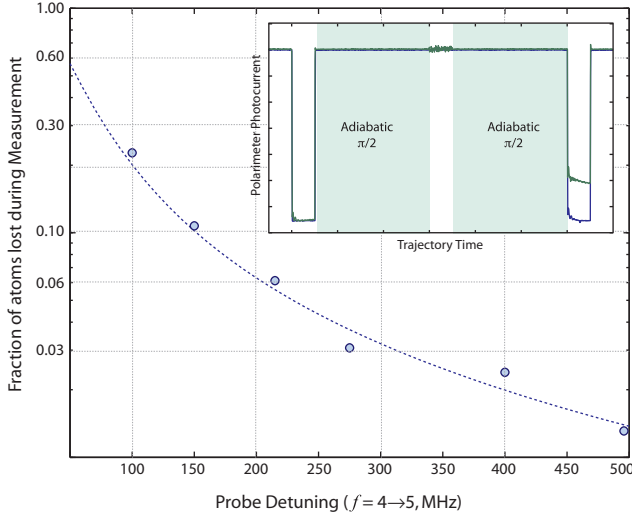


FIG. 9: (color online) Measure of the atomic decoherence due to atom loss by non-paraxial scattering of probe light as a function of probe detuning at fixed power, $P = 100$ W and duration $\tau = 100$ s. The dotted line represents the predictions of a first order decay model with a scattering rate that accounts for multiple excited state hyperfine levels. The inset describes the procedure used to measure the atom loss (refer to text).

C. Verifying the Small Decoherence Limit

In order to verify that we were indeed operating in a small decoherence limit, we compared measurements of the atom loss to the predictions of a first order model, $N(t) = \exp(-\kappa_s t)$, where the atom loss rate,

$$\kappa_s = \frac{X}{f^0} \frac{(\kappa_f f^0)}{\sim!} I_p \quad (63)$$

is determined by the probe laser intensity, I_p , and the atomic scattering cross sections, $(\kappa_f f^0)$. This model of atom loss due to probe induced decoherence has been considered previously [18] and we have trivially extended the expression to include multiple excited atomic hyperfine states.

Experimentally, atom loss was measured in the following manner (refer to the inset plot in Fig. 9). Following atom trapping, cooling and optical pumping, the atomic magnetization vector was adiabatically rotated to be parallel with the positive z -axis ($\theta = 0$). The probe light shutter was then opened for a 100 s period after which the probe light was turned off and the atoms adiabatically rotated back to the x -axis ($\theta = \pi/2$, $\phi = 0$). The probe light was enabled for 100 s after which the atoms were once again adiabatically rotated to the z -axis ($\theta = 0$). With the atomic magnetization polarized along the z -axis, the polarimeter photocurrent provides a measure of the atom number. Therefore, comparing the polarimeter output for the two z -axis measurement periods yields an estimate of the atom loss induced by

the middle x -axis probe period. In order to calibrate signal loss between the two z -axis measurement periods in the absence of probe-induced decoherence, this procedure was repeated but without the middle x -axis measurement period. The fractional atom loss was computed from the ratio of the average photocurrents obtained in the final 100 s probe windows for the two (center measurement and no center measurement) procedures. A comparison of the measured and predicted atom loss as a function of probe detuning for a constant power $P = 100$ W and measurement duration 100 s is plotted in Fig. 9.

V. PROCEDURE FOR ABSOLUTE SQUEEZING CALIBRATION

To analyze conditional spin-squeezing, we considered statistical ensembles of photocurrents (acquired in the absence of magnetic driving),

$$Y_t^{(\text{expt})} = Y_t^{(1)}; Y_t^{(2)}; \dots; Y_t^{(S)}; \quad 0 \leq t \leq 2 \quad (64)$$

Within each ensemble, all experimental parameters, including the atom number, volume, probe power and detuning, were fixed. As indicated by the time-domain limits, $t = [0; 2]$, the photocurrents in Eq. (64) are twice as long as the intended measurement duration, τ , for reasons which will become clear shortly.

Under these conditions, the photocurrents in Y_t assume the (ideal) form in Eq. (8) and their time-averages yield an ensemble of associated measurement outcomes,

$$Y_{[0; 2]}^{(\text{expt})} = Y_{[0; 2]}^{(1)}; Y_{[0; 2]}^{(2)}; \dots; Y_{[0; 2]}^{(S)}; \quad (65)$$

In a quantum-limited experiment, the variance of $Y_{[0; 2]}^{(\text{expt})}$ is due to a combination of the coherent spin state spin uncertainty, the measurement noise, and the polarimeter photodetector properties. The variance of the underlying shot-to-shot photocurrent means, $h p^2(y)$, can be obtained from the Gaussian statistics of the measurement ensemble,

$$h p^2(y) = \text{var} Y_{[0; 2]}^{(\text{expt})} = g^2 \frac{\sigma^2}{2}; \quad (66)$$

where σ is defined in Eq. (50), g is the responsivity of the polarimeter photodetectors and g is the transimpedance gain (refer to Section IV B). As expected, shot-to-shot quantum fluctuations in the z -component of the atomic spin are compounded by incomplete photocurrent averaging (refer to Sec. III). Thus, $h p^2(y)$ in Eq. (66) can be interpreted as the shot-to-shot photocurrent fluctuations due to pure quantum uncertainty in the initial spin state (ideally a coherent state) revealed by subtracting off the known amount of residual measurement noise.

1. Conditional Photocurrent Statistics

The distribution $p(y)$ does not provide information about the degree of conditioning produced by the continuous measurement. Toward this end, we divided each photocurrent in the ensemble, $y_t^{(s)}$, into two parts,

Measurement Period 1 of each trajectory is associated with the first half of the photocurrent, $y_t^{(1)}$, where $0 \leq t < \frac{1}{2}$. The statistical ensemble of measurement outcomes corresponds to the mean values,

$$Y_{[0;1]} = \langle Y_{[0;1]}^{(1)}, Y_{[0;1]}^{(2)}, \dots, Y_{[0;1]}^{(S)} \rangle^T : \quad (67)$$

Measurement Period 2 of each trajectory is associated with the second half of the photocurrent, $y_t^{(2)}$, where $\frac{1}{2} \leq t < 1$. The statistical ensemble of measurement outcomes corresponds to the mean values,

$$Y_{[1;2]} = \langle Y_{[1;2]}^{(1)}, Y_{[1;2]}^{(2)}, \dots, Y_{[1;2]}^{(S)} \rangle^T : \quad (68)$$

This (somewhat arbitrary) division allows us to assess the degree of spin-squeezing from the variance of the conditional photocurrent distribution,

$$p(Y_{[1;2]} | Y_{[0;1]}) = p(Y_{[1;2]} - Y_{[0;1]}) ; \quad (69)$$

interpreted as the uncertainty in how well one can predict the second measurement outcome, $y_{[1;2]}$, given that the outcome of the first measurement period yielded $y_{[0;1]}$. The variance of this distribution can be obtained from the statistics of the measured photocurrents,

$$h p^2(Y_{[1;2]} | Y_{[0;1]}) i / h^2 p(Y_{[1;2]} - Y_{[0;1]}) i \quad (70)$$

$$h p^2(Y_{[1;2]} | Y_{[0;1]}) i = \frac{1}{2} \left(1 + \frac{SNR^2}{h^2} \right) \frac{i}{\text{var } Y_{[1;2]}^{(\text{expt})} - Y_{[0;1]}^{(\text{expt})}} \quad (70)$$

where the equality in the second line is obtained by using Eq. (66) in conjunction with the following identity for the (measured) signal-to-noise ratio,

$$SNR^2 = \frac{1}{2} \frac{\frac{h}{\text{var } Y_{[0;1]}^{(\text{expt})}} + \frac{h}{\text{var } Y_{[1;2]}^{(\text{expt})}}}{\frac{h}{\text{var } Y_{[1;2]}^{(\text{expt})}} - \frac{h}{\text{var } Y_{[0;1]}^{(\text{expt})}}} \frac{i}{A} ; \quad (71)$$

that is readily obtained from the Gaussian statistics of y and \hat{y} as described in Section III. Finally, the degree of uncertainty reduction relative to the initial spin state is obtained from the variance ratio,

$$W = \frac{h p^2(Y_{[1;2]} | Y_{[0;1]}) i}{h p^2(y) i} : \quad (72)$$

A. Absolute Calibration Procedure

One could compute the degree of squeezing by evaluating Eq. (72) using only experimentally characterized statistics, but that would not provide an independent calibration | it fails to reference any independent measure of the coherent spin state fluctuations. To do so, the measured conditional photocurrent statistics should be compared against a theoretical prediction of the coherent state-equivalent photocurrent variance obtained from the input-output formalism of the scattering process and an independent determination of M .

Comparing measured quantities against a theoretical benchmark is an essential component of an independent calibration that avoids attributing actual spin-squeezing to what is really a reduction in residual classical uncertainty. Indeed, many classical noise sources, including background magnetic field fluctuations, are capable of increasing the observed shot-to-shot photocurrent variance, and perfect preparation of a true minimum uncertainty state by optical pumping is unlikely. That is, the measured unconditional variance, $h p^2(y) i$, might be larger than that of a true coherent spin state and would artificially enhance the squeezing predicted by Eq. (72).

Rather, the ratio in Eq. (72) should be evaluated using an independently calibrated theoretical reference value for the coherent state equivalent photocurrent variance,

$$W^{(\text{abs})} = \frac{h p^2(Y_{[1;2]} | Y_{[0;1]}) i}{h p^2(y) i^{(\text{abs})}} : \quad (73)$$

readily derived from Eq. (42),

$$h p^2(y) i^{(\text{abs})} = \frac{g^2}{2} M h F_z^2 i \quad (74) \\ = \frac{F}{2} \frac{3}{4} \frac{\frac{3}{2} P g}{4^2 r^2} X \frac{(1)}{f;f^0} \frac{3_2}{5} :$$

B. Experimental Results

The desired photocurrents were obtained by carefully nulling residual background magnetic fields as described in Section IV A. For each measurement trajectory, atoms were collected into the MOT, sub-Doppler cooled to 5

K, and optically pumped in the presence of a 100 mG holding magnetic field oriented along the x-axis. Following optical pumping, the 100 mG x-axis holding field was maintained for 20 ms to allow all other transient magnetic fields to subside.

At this point, the probe shutter was opened and the photocurrent was recorded beginning 20 s after the probe trigger. This short delay between the onset of the probe light and the beginning of the conditional measurement record was necessary to avoid transient settling of the polarimeter photodetectors immediately after enabling the probe light. The first 100 s of the acquired

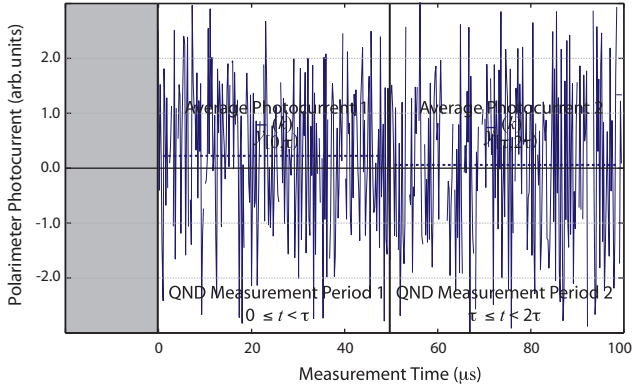


FIG. 10: (color online) Example photocurrent for a measurement with duration $\tau = 50$ s, probe power $P = 100$ W and detuning $\delta = 150$ MHz. Each trajectory is divided into two consecutive periods, $0 \leq t < \tau$ and $\tau \leq t < 2\tau$, which define two measurement outcomes, $y_{[0,1]}$ and $y_{[1,2]}$, given by the average photocurrent during each period.

photocurrent provided the measurement, after which resonant light from the trapping lasers was used to rapidly disperse the atoms. Once the sample was destroyed, the residual offset (averaged in a 50 ms window) on the polarimeter photocurrent was subtracted from the entire photocurrent for that trajectory to further suppress shot-to-shot DC fluctuations in the polarimeter output.

1. Absolute Calibration

Ensembles containing $S = 500$ photocurrents were acquired for five different probe detunings, $\delta = 100, 150, 200, 300$, and 400 MHz. In all ensembles, the optical power, atom number and volume were fixed at $P = 100$ W, $N = 3 \times 10^9$ and $r = 4$ mm. An example trajectory acquired according to the above procedure (for $\delta = 150$ MHz) is depicted in Fig. 10. The figure indicates the two consecutive $\tau = 50$ s measurement periods used to compute conditional statistics from the average photocurrent in each period, $y_{[0,1]}^{(s)}$ and $y_{[1,2]}^{(s)}$, as described above. Example histograms of the probability distributions, $p(y)$ and $p(y_{[1,2]} | y_{[0,1]}^{(s)})$, for the $\delta = 150$ MHz ensemble are depicted in the inset of Fig. 11.

Absolute spin-squeezing calibrations were computed for each of the 5 measurement ensembles using Eq. (73), and the results are summarized in Fig. 11 and Table I. The reported errorbars reflect statistical sampling uncertainty in the experimentally characterized conditional probability distribution, $p(y_{[1,2]} | y_{[0,1]}^{(s)})$. It should be noted that there is a small possibility of systematic uncertainty in the measured atom number used to compute the theoretical coherent state variance as well as the optical pumping efficiency (discussed below). Such effects were minimized by operating the experiment with a sufficiently low optical depth to allow efficient opti-

cal pumping. Atom number uncertainty was estimated $< 20\%$ based on fluorescence measurements performed over a wide range of excitation powers and detunings.

Table I also provides the results of a squeezing calibration computed using the measured initial state variance in Eq. (66) to evaluate Eq. (72). The observation that these relative calibrations indicate greater squeezing than $W^{(\text{abs})}$ suggests that the initial optically pumped state is not (as expected) a perfect coherent state; however, since we observe calibrations, $W^{(\text{abs})} < 1$, we can conclude that quantum squeezing is occurring.

Not surprisingly, we observe less squeezing than the theoretical achievable maximum (solid curve in Fig. 11 computed from the theoretical signal-to-noise ratio). For comparison, this limit is also plotted for probe powers of $P = 50$ W and $P = 25$ W. The finding that we approach, but do not exactly achieve, the in-principle degree of squeezing is to be reasonably expected. Possible sources of excess technical noise in our experiment arise from imperfect DC balancing of our polarimeter photocurrent coupled with broadband technical noise on our probe laser imparted by the acousto-optic modulator (shutter). Additional uncertainty results from residual ambient magnetic field fluctuations not cancelled by our active trim coils or passive shielding. Field fluctuations result in slight, random atomic Larmor precession which manifests itself as an increased variance in the spin measurement statistics. More fundamentally, albeit small (6.8%), atom loss due to probe-induced decoherence from non-paraxial scattering introduces a systematic reduction in $y_{[1,2]}$, since the effective atom number is smaller.

C. Discussion

Our spin-squeezing calibration requires an accurate inference of the theoretical coherent state photocurrent variance from the atom number, N , volume, V , probe power, P , and detuning, δ . In practice, the least certain of these determinations is that of N . In fact we have an independent check on this parameter from the Stokes vector measurements described in Sec. IV B, which yield an estimate of the total atomic magnetization, F_j . Given perfect optical pumping we would expect $F_j = N_f$; a direct comparison of our fluorescence measurement of N with our Stokes measurement of F_j suggests an actual optical pumping efficiency $\sim 90\%$, consistent with expec-

TABLE I: Conditional spin-squeezing calibration results for $N = 3 \times 10^9$, $V = 4$ mm 3 , and $P = 100$ W.

(MHz)	$W^{(\text{abs})}$ (dB)	$W^{(\text{expt})}$ (dB)
100	3.1 0.1	6.4 0.15
150	2.0 0.1	3.1 0.15
200	1.6 0.1	1.2 0.15
300	0.9 0.1	1.1 0.15
400	0.5 0.1	0.4 0.15

tations for our experimental conditions.

Ideally, one would perform an independent characterization of the pumping efficiency [28] for further verification. However, in the absence of such, we reduced the potential for systematic error in our optical pumping by operating the experiment with a significantly reduced atom number and optical depth compared to our previous work [7]. These experimental conditions intentionally bring us closer to our technical noise floor and reduce the degree of observed conditional squeezing in exchange for increased confidence in our calibration. As such, these current results do not maximize our squeezing capability, which will be addressed in a following work.

Finally it is worth noting that one might additionally account for non-minimum-uncertainty initial spin states [11], as would be the case for imperfect optical pumping. Doing so would be accomplished by adjusting the theoretical variance, $h F_z^2 i$, in the independent squeezing calibration expressions to reflect that of the actual initial spin state. For quantum information applications, where the precise degree of atomic entanglement is of interest, the initial atomic state must be well known.

However, it is not clear that there is much to gain from such an analysis in precision metrological applications. Specifically, in any feedback stabilized spin-resonance measurement, increased robustness to both excess quantum and classical fluctuations implies that the uncertainty of the measurement is limited by the averaged photocurrent variance more so than any other

statistic [42]. As such, suppressing the effects of coherent state quantum projection noise limit in a closed-loop parameter estimation context only requires that the latter uncertainty fall below the coherent state level, the starting conditions are immaterial to within reason.

VII. CONCLUSION

We developed a model for describing conditional spin-squeezing in alkali atoms. Achieving quantitative agreement between theory and experiment was accomplished by treating in detail the optical probe scattering process at the heart of the measurement. We found that an adequate comparison was only possible after including all relevant hyperfine transitions including their relative (non-unit) oscillator strengths in our model of the atomic physics, but that it was sufficient to work within a semiclassical treatment of the collective atomic spin. Furthermore, we demonstrated the advantages of a quantum trajectory and filtering theory treatment of the measurement conditioning process.

Detailed investigation of the atom probe scattering physics indicates that it is possible to eliminate unwanted tensor components of the atomic polarizability by adopting a suitable atomic and optical polarization geometry. This includes the elimination of dephasing due to the quadratic light shift [29] without sacrificing a fixed laboratory coordinate system for the measurement. Moreover, we found that conditional spin-squeezing experiments could be performed at small optical detunings without a qualitative change in the form of the photocurrent (in the small decoherence limit). Reducing decoherence for free-space atom-field coupling at a fixed detuning can only be achieved by reducing the probe power or equivalently shortening the measurement duration.

Due to the close agreement between theoretical predictions and experimental data, it is reasonable to believe that these results provide the first independent calibration of conditional spin-squeezing in an atomic ensemble. All indications suggest that the amount of squeezing we can achieve is limited chiefly by residual technical noise in our experiment that lies above the intrinsic quantum fluctuations and we are working to further reduce these effects. But, we believe that it is now possible to approach applications in precision spin resonance measurements, such as atomic magnetometry, with increased confidence that one can outperform the shotnoise detection limit.

Acknowledgments

The authors would like to thank Poul Jessen, Ivan Deutsch, Andrew Silberfarb, Dimitri Budker and especially Ramon van Handel and Andrew Doherty for numerous insightful discussions. This work was supported by the Caltech MURIC center for Quantum Networks (DAAD19-00-1-0374). JM G acknowledges support from the Caltech

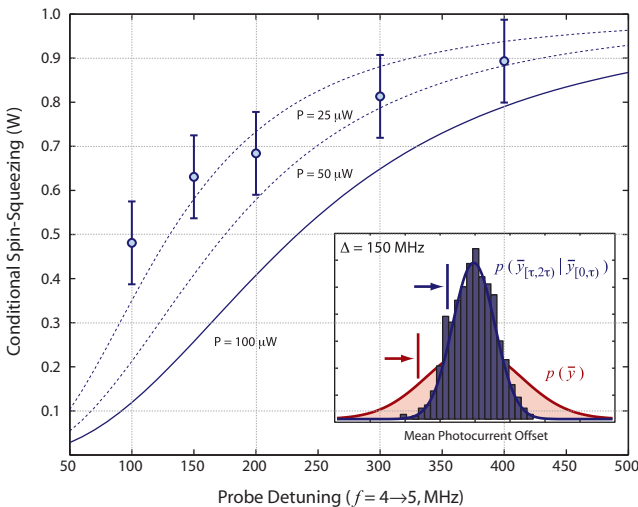


FIG. 11: (color online) The degree of spin-squeezing, measured as the fractional reduction of the conditional measurement variance, $p(y_{1,2} | y_{0,1})$, relative to an independent prediction of the coherent state-equivalent photocurrent variance. Statistics were acquired from 500 continuous measurement trajectories per data point with a fixed probe power of 100 μW , atom number of $N = 3 \times 10^9$ and trap volume of $r = 4 \text{ mm}$. Curves indicate the expected degree of squeezing for different probe optical powers computed from the theoretical signal to noise ratio for the indicated experimental parameters.

[1] V. Braginski and F. Khalili, *Quantum Measurements* (Cambridge University Press, 1992).

[2] M. Kitagawa and M. Ueda, *Phys. Rev. A* 47, 5138 (1993).

[3] M. Brune, S. Haroche, V. Lefevre, J. Raimond, and N. Zagury, *Phys. Rev. Lett.* 65, 976 (1990).

[4] G. Nogues, A. Rauschenbeutel, S. Osnaghi, M. Brune, J. Raimond, and S. Haroche, *Nature* 400, 239 (1999).

[5] A. Kuzmich, L. Mandel, and N. P. Bigelow, *Phys. Rev. Lett.* 85, 1594 (2000).

[6] B. Julsgaard, A. Kozhekin, and E. S. Polzik, *Nature* 413, 400 (2001), URL quant-ph/0106057.

[7] J. Gherem ia, J. K. Stockton, and H. Mabuchi, *Science* 304, 270 (2004).

[8] J. Gherem ia, J. K. Stockton, and H. Mabuchi (2005), URL quant-ph/0401107.

[9] J. K. Stockton, J. Gherem ia, A. C. Doherty, and H. Mabuchi, *Phys. Rev. A* 67, 022122 (2003), URL quant-ph/0210117.

[10] A. S. renzen, L. M. Duan, J. Cirac, and P. Zoller, *Nature* 63, 409 (2001), URL quant-ph/0006111.

[11] A. S. renzen and K. M. Mørk, *Phys. Rev. Lett.* 86, 4431 (2001).

[12] D. J. Wineland, J. J. Bollinger, W. M. Itano, and D. J. Heinzen, *Phys. Rev. A* 50, 6788 (1994).

[13] J. Gherem ia, J. K. Stockton, A. C. Doherty, and H. Mabuchi, *Phys. Rev. Lett.* 91, 250801 (2003), URL quant-ph/0306192.

[14] A. Andre, A. S. renzen, and M. Lukin, *Phys. Rev. Lett.* 92, 230801 (2004).

[15] V. Peterson, L. B. Madsen, and K. M. Mørk, *Phys. Rev. A* 71, 012312 (2005), URL quant-ph/0409202.

[16] B. Julsgaard, J. Sherson, J. Sørensen, and E. Polzik, *J. Opt. B: Quantum Semiclass. Opt.* 6, 5 (2004), URL quant-ph/0307028.

[17] W. Happer, *Rev. Mod. Phys.* 44, 169 (1972).

[18] G. A. Smith, S. Chaudhury, and P. S. Jessen, *J. Opt. B: Quant. Semiclass. Opt.* 5, 323 (2003), URL quant-ph/0304163.

[19] Y. Takahashi, K. Honda, N. Tanaka, K. Toyoda, K. Ishikawa, and T. Yabuzaki, *Phys. Rev. A* 60, 4974 (1999).

[20] A. Kuzmich, N. Bigelow, and L. Mandel, *Europhys. Lett.* 42, 481 (1998).

[21] L. K. Thomsen, S. Mancini, and H. M. Wiseman, *Phys. Rev. A* 65, 061801 (2002), URL quant-ph/0202028.

[22] L. K. Thomsen and H. M. Wiseman, *Phys. Rev. A* 65 (2002), URL quant-ph/0202027.

[23] L. K. Thomsen, S. Mancini, and H. M. Wiseman, *J. Phys. B: At. Mol. Opt. Phys.* 35, 4937 (2002), URL quant-ph/0208160.

[24] A. Silberfarb and I. D. Dutsch, *Phys. Rev. A* 68, 013817 (2003), URL quant-ph/0210056.

[25] C. Gardiner, *Quantum Noise* (Springer Verlag, 1991).

[26] R. van Handel, J. K. Stockton, and H. Mabuchi, *IEEE Trans. Autom. Control*, to appear (2004), URL quant-ph/0402093.

[27] J. Gough, *Commun. Math. Phys.* p. 10.1007 (2004).

[28] D. Kupriyanov, O. M. Ishina, I. Sokolov, B. Julsgaard, and E. Polzik (2004), URL quant-ph/0411083.

[29] G. A. Smith, S. Chaudhury, A. Silberfarb, I. H. Dutsch, and P. S. Jessen, *Phys. Rev. Lett.* 93, 163602 (2004), URL quant-ph/0403096.

[30] A. Silberfarb, P. S. Jessen, and I. H. Dutsch (2005), quant-ph/0412032.

[31] W. Happer and B. M. Athur, *Phys. Rev. Lett.* 163, 12 (1967).

[32] I. H. Dutsch and P. Jessen, *Phys. Rev. A* 57, 1972 (1998).

[33] H. Nha and H. Carmichael, *Phys. Rev. A* 71, 013805 (2005), URL quant-ph/0411007.

[34] L. Accardi, L. Frigerio, and Y. Lu, *Commun. Math. Phys.* 131, 537 (1990).

[35] L. V. Hove, *Physica* 21, 617 (1955).

[36] C. Cohen-Tannoudji, J. Dupont-Roc, and G. Grynberg, *Atom Photon Interactions* (Wiley-Interscience, New York, 1992).

[37] I. Carusotto and E. J. Mueller, *J. Phys. B* 37, S115 (2004).

[38] R. Glauber, *Phys. Rev. Lett.* 131, 2766 (1963).

[39] L. Mandel and E. Wolf, *Optical Coherence and Quantum Optics* (Cambridge University Press, 1995).

[40] H. M. Wiseman and G. J. Milburn, *Phys. Rev. A* 47, 642 (1993).

[41] D. Oblak, J. K. Mikkelsen, W. Tittel, A. K. Vershovski, J. L. Sørensen, P. G. Petrov, C. L. G. Alzar, and E. S. Polzik (2003), URL quant-ph/0312165.

[42] J. K. Stockton, J. Gherem ia, A. C. Doherty, and H. Mabuchi, *Phys. Rev. A* 69, 032109 (2004), URL quant-ph/0309101.

[43] P. L. Gould and H. J. M. Etcalf, *Phys. Rev. Lett.* 61, 169 (1988).

APPENDIX A : THE POLARIZABILITY SCATTERING HAMILTONIAN AND ITS REDUCIBLE REPRESENTATIONS

We begin our description of the atom field scattering process from the familiar atom field polarizability Hamiltonian [17, 32, 36],

$$\hat{H} = \hat{E}^{(+)}(\mathbf{r}; t) \frac{\hat{d} \hat{d}^{\dagger}}{\sim} \hat{E}^{(+)}(\mathbf{r}; t) \quad (A1)$$

where \hat{d} is the vector atomic dipole operator and $\hat{E}^{(+)}$ and $\hat{E}^{(-)}$ are the positive and negative frequency components of the probe field operators. This notation, involving \hat{d}^{\dagger} and \hat{d} (which are Hermitian so $\hat{d} = \hat{d}^{\dagger}$), has been adopted to suggest that the dipole operator assumes the dual roles of atomic raising and lowering operators. \hat{d}^{\dagger} and \hat{d} connect the ground and excited atomic states via coupling with the probe electric field.

This Hamiltonian has the following physical interpretation that makes it particularly appropriate for addressing scattering problems: two different field modes couple

to the atom via a short-lived (or virtual) atom is excited state. A probe photon is first annihilated, thus driving the atom to a virtual excited state followed by emission into a new field mode resulting in potentially different internal atomic and probe states.

With this picture in mind, it is beneficial to expand the dipole operators,

$$\hat{d}^y = \sum_{f^0 m^0}^X \sum_{f^0 m^0}^X \sum_{f^0 m^0}^X \hat{f}^0; m^0 i \hat{h}^0; m^0 i \hat{f}^0; m^0 i \hat{f}^0; m^0 i \quad (A 2)$$

in the basis of Zeeman degenerate atomic hyperfine states, $\hat{f}; m i$. Here f and f^0 are the total spin quantum numbers for the ground and excited hyperfine levels while m and m^0 are their projections on the z -axis. That is to say, $\hat{f}; m i$ are eigenstates of the total atomic angular momentum,

$$\hat{f} = \hat{s} \hat{\mathbf{l}}_1 \hat{\mathbf{l}}_i + \hat{\mathbf{l}}_s \hat{\mathbf{l}}_i + \hat{\mathbf{l}}_s \hat{\mathbf{l}}_i \quad (A 3)$$

where \hat{s} , $\hat{\mathbf{l}}$, and $\hat{\mathbf{l}}_i$ are respectively the electron spin, orbital angular momentum, and the nuclear spin. The quantum numbers, f , and m , are defined in the usual manner,

$$\begin{aligned} \hat{f}^2; m i &= \sim^2 f (f + 1) \hat{f}; m i \\ \hat{f}_z \hat{f}; m i &= \sim m \hat{f}; m i \end{aligned} \quad (A 4)$$

Substituting Eq. (A 2) into the effective Hamiltonian gives us,

$$\begin{aligned} \hat{H} &= \sum_{f^0 m^0 m^0 m^0}^X \sum_{f^0 m^0 i}^X \hat{f}; m^0 i \hat{h}^0; m^0 i \hat{f}^0; m^0 i \hat{f}^0; m^0 i \\ &\quad \hat{h}^0; m^0 i \hat{f}^0; m^0 i \hat{f}^0; m^0 i \end{aligned} \quad (A 5)$$

It involves dipole matrix elements of the form, $\hat{h}^0; m^0 i \hat{f}^0; m^0 i$ where $\hat{f}; m i$ is a Zeeman sub-level in the ground-state hyperfine manifold, $\hat{f}^0; m^0 i$ is a virtual state in the excited hyperfine manifold, and $q = 0; \pm 1$ labels the helicity of the electromagnetic field.

In order to work with this expression, it is advantageous to first simplify these dipole matrix elements as far as possible. By employing the Wigner-Eckart theorem, the angular dependence of the matrix element, $\hat{h}^0; m^0 i \hat{f}^0; m^0 i$ can be factored into the product of a Clebsch-Gordan coefficient and a reduced matrix element,

$$\hat{h}^0; m^0 i \hat{f}^0; m^0 i = \hat{h}^0; m^0 + q \hat{J}; q; f; m^0 i \hat{h}^0; j \hat{J}; j i \quad (A 6)$$

Since the dipole operator acts only on electronic degrees of freedom, it is further possible to factor out the nuclear spin degrees of freedom via the explicit coupling,

$$\begin{aligned} \hat{h}^0; j \hat{J}; j i &= h(i; j^0) \hat{f}^0; j \hat{J}; j i \hat{f}^0; j \hat{J}; j i \\ &= \left(\begin{array}{c} 1 \\ 1 \end{array} \right) \left(\begin{array}{c} f^0 \\ f^0 \end{array} \right) \left(\begin{array}{c} m^0 \\ m^0 \end{array} \right) \left(\begin{array}{c} i \\ i \end{array} \right) \frac{h(i; j^0) \hat{f}^0; j \hat{J}; j i}{(2f + 1)(2j^0 + 1)} \end{aligned} \quad (A 7)$$

where i is the nuclear spin quantum number and \hat{d}_e is the dipole operator with respect to the electronic degrees of freedom. Finally, the dipole matrix elements can be expressed as,

$$\begin{aligned} \hat{h}^0; m^0 i \hat{f}^0; m^0 i &= \left(\begin{array}{c} 1 \\ 1 \end{array} \right) \left(\begin{array}{c} f^0 \\ f^0 \end{array} \right) \left(\begin{array}{c} m^0 \\ m^0 \end{array} \right) \frac{h^0; j \hat{J}; j i}{(2f + 1)(2j^0 + 1)} \\ &= \hat{h}^0; j \hat{J}; j i \end{aligned} \quad (A 8)$$

By invoking the selection rules imposed by the Clebsch-Gordan triangle inequality, the atomic raising operator takes on the simplified form,

$$\begin{aligned} \hat{d}_q^y &= \left(\begin{array}{c} 1 \\ 1 \end{array} \right) \left(\begin{array}{c} f^0 \\ f^0 \end{array} \right) \left(\begin{array}{c} m^0 \\ m^0 \end{array} \right) \frac{h^0; j \hat{J}; j i}{(2f + 1)(2j^0 + 1)} \\ &= \hat{h}^0; j \hat{J}; j i + \hat{q} \hat{h}^0; j \hat{J}; j i \end{aligned} \quad (A 9)$$

We will find it convenient to define the following two sets of constants that will aid in simplifying the atomic polarizability expressions to follow. The first of these is,

$$\alpha_0 = \frac{3}{8} \alpha \quad (A 10)$$

which involves the atomic spontaneous emission rate, α , and transition wavelength, λ_0 . The second constant reflects the oscillator strengths of the different hyperfine transitions that contribute to the polarizability tensor,

$$\alpha_f = \frac{(2f + 1)(2j^0 + 1)^2}{(2j + 1)} \left(\begin{array}{c} 1 \\ 1 \end{array} \right) \left(\begin{array}{c} f^0 \\ f^0 \end{array} \right)^2 \quad (A 11)$$

where j and j^0 , the ground and excited state fine structure quantum numbers.

1. Irreducible Spherical Tensor Decomposition

The irreducible spherical tensor contributions to the atomic polarizability are identified by decomposing the dyadic $\hat{d} \hat{d}^y$ into the direct sum of a scalar, vector, and symmetric tensor,

$$\hat{H} = \hat{H}^{(0)} + \hat{H}^{(1)} + \hat{H}^{(2)} \quad (A 12)$$

in its 3-space representation. Motivated by these rotational symmetry properties, our goal is to identify operators in the atomic Hilbert space corresponding to this decomposition. That will allow us to write the atomic polarizability Hamiltonian as a sum,

$$\hat{H} = \hat{H}^{(0)} + \hat{H}^{(1)} + \hat{H}^{(2)} \quad (A 13)$$

over terms that correspond to the different respective rotational symmetries of the polarizability tensor. In their Hilbert space representation, the terms contributing to the scattering Hamiltonian will not commute with one

another.

Rank-0 Component. The scalar, or rank-0, contribution to the dyadic $\hat{d}\hat{d}^y$, can be obtained from the inner product of \hat{d} and \hat{d}^y ,

$$\hat{T}_0^{(0)} = \frac{1}{3} \hat{d} \hat{d}^y = \frac{1}{3} \hat{d}_0 \hat{d}_0^y \quad \hat{d}_+ \hat{d}^y \quad \hat{d} \hat{d}_+^y \quad : \quad (A14)$$

which can be related to the ground state atom in angular momentum operators using recursion relation expressions for the Clebsch-Gordan coefficients. After some algebra, the elements of the rank-0 spherical tensor operator can be expressed as,

$$\hat{T}_0^{(0)} = \frac{1}{3}^h (2f-1) \frac{f}{f} \frac{f^0+1}{f} + (2f+1) \frac{f}{f} \frac{f^0}{f} (A15) \\ + (2f+3) \frac{f+1}{f} \frac{f^0-1}{f} \hat{\mathbb{I}}_f$$

where $\frac{f^0}{f}$ is the Kronecker delta and we have adopted the convention that repeated indices are summed.

To obtain the full representation of the rank-0 atom \mathbf{ic} polarizability, we must properly sum the contributions corresponding to the three spherical basis vectors,

$$\begin{aligned}
 \hat{\wedge}^{(0)} &= 0 \begin{smallmatrix} q^0 \\ q \\ 0 \end{smallmatrix} \mathbf{e}_q \mathbf{e}_q \hat{\mathbf{T}}_0^{(0)} & (A.16) \\
 &= 0 \begin{smallmatrix} B \\ \mathbf{e} \end{smallmatrix} \hat{\mathbf{T}}_0^{(0)} \begin{matrix} 0 \\ 0 \\ 0 \end{matrix} \begin{smallmatrix} C \\ \mathbf{A} \end{matrix} \\
 &= 0 \begin{smallmatrix} X \\ f^0 \end{smallmatrix} \begin{smallmatrix} (0) \\ f; f^0 \end{smallmatrix} \mathbf{e} \mathbf{e} + \mathbf{e}_0 \mathbf{e}_0 + \mathbf{e}_+ \mathbf{e}_+ \hat{\mathbf{f}}_f
 \end{aligned}$$

having defined the unitless polarizability coefficient,

$$\begin{matrix} (0) \\ f; f^0 \end{matrix} = \frac{1}{3} (2f-1) \begin{matrix} f & 1 & f^0+1 \\ f & f & f \end{matrix} \quad (\text{A } 17)$$

These spherical tensor operators can be appropriately expanded as an outer product of spherical basis vectors,

$$\begin{aligned}
& \wedge^{(1)} = \begin{pmatrix} 0 & \mathbf{e}_q \mathbf{e}_q^0 & q^0 & q \mathbf{e}_q^0 & q^0 \mathbf{e}_q^0 & \hat{T}_{q^0}^{(0)} \\ 0 & 0 & 0 & 0 & 0 & 0 \end{pmatrix} \quad (A 20) \\
& = \begin{pmatrix} \frac{1}{2} & 0 & \mathbf{B} & 0 & \frac{p}{2} \hat{T}_0^{(1)} & i \frac{p}{2} \hat{T}_0^{(1)} \\ 0 & 0 & 0 & 0 & 0 & \hat{T}_+^{(1)} + \hat{T}^{(1)} \\ 0 & \frac{p}{2} \hat{T}_0^{(1)} & 0 & 0 & 0 & i(\hat{T}_+^{(1)} + \hat{T}^{(1)}) \frac{C}{A} \\ 0 & 0 & 0 & 0 & 0 & 0 \end{pmatrix} \\
& = \begin{pmatrix} X & \frac{1}{h} & \hat{T}_+^{(1)} + \hat{T}^{(1)} & i(\hat{T}_+^{(1)} + \hat{T}^{(1)}) & 0 & 0 \\ 0 & f_+ f^0 & \mathbf{e}_0 \mathbf{e}_0^0 & \mathbf{e}_+ \mathbf{e}_0 & \hat{f} & \frac{p}{2} \mathbf{e}_+ \mathbf{e}_+^0 \\ 0 & f^0 & 0 & 0 & 0 & \mathbf{e}_+ \mathbf{e}_+^0 + \mathbf{e}_0 \mathbf{e}_0^0 + \mathbf{e}_0 \mathbf{e}_+ + \mathbf{e}_+ \mathbf{e}_0 \end{pmatrix} \quad i
\end{aligned}$$

where ϵ_{ijk} is the completely anti-symmetric tensor (Levi-Civita symbol) and we have defined the rank-1 characteristic atomic polarizability,

$$\frac{(1)}{f; f^0} = \frac{1}{p} = \frac{2f}{f} \frac{1}{f} \frac{f}{f} \frac{1}{f} \frac{f^0 + 1}{f} + \frac{2f + 1}{f(f + 1)} \frac{f}{f} \frac{f^0}{f}$$

$$+ (2f+1) \frac{f}{f} \frac{f^0}{f} + (2f+3) \frac{f+1}{f} \frac{f^0}{f} \quad ;$$

and made use of Eqs. (A 10) and (A 11).

Rank-1 Component. The rank-1 spherical tensor contribution to the atom's polarizability contains three components. Again, by invoking the definitions of the Clebsch-Gordan coefficients and after a good deal of algebra, it is possible to relate the resulting spherical tensor operators to the atom's ground state angular momentum operators,

$$\begin{aligned}
 \hat{T}^{(1)} &= \frac{i}{p-2} \hat{d} \hat{d}_0^Y \hat{d}_0 \hat{d}^Y \\
 &= \frac{1}{p-2} \frac{2f-1}{f} \frac{f-1}{f} \frac{f^0+1}{f} + \frac{2f+1}{f(f+1)} \frac{f-f^0}{f} \\
 &\quad \frac{2f+3}{f+1} \frac{f+1}{f} \frac{f^0-1}{f} \hat{f}
 \end{aligned} \tag{A 18)$$

where

$$\begin{aligned}
 \hat{T}_0^{(1)} &= \frac{i}{\hat{p} \frac{1}{2}} \hat{d} \hat{d}_+^{\dagger} \hat{d}_+ \hat{d}_+^{\dagger} \quad (\text{A 19}) \\
 &= \frac{1}{\hat{p} \frac{1}{2}} \frac{2f-1}{f} \frac{f-1}{f} \frac{f^0+1}{f} + \frac{2f+1}{f(f+1)} \frac{f}{f} \frac{f^0}{f} \\
 &\quad \frac{2f+3}{f+1} \frac{f+1}{f} \frac{f^0-1}{f} \hat{f}_z:
 \end{aligned}$$

$$\frac{2f+3}{f+1} \quad \begin{matrix} f+1 & f^0 & 1 \\ f & f \end{matrix} \quad (A\ 21)$$

Evidently, the rank-1 polarizability couples the different spherical polarization components of the radiation field to atomic spin operators. It is this contribution to the atom-probe scattering Hamiltonian that is re-

sponsible for Faraday rotation. That is, the interaction in parts a di erential phase shift on the di erent circular components that is proportional to the z-component of the atom ic spin angular momentum .

Rank-2 Component. Finally we consider the symmetric rank-2 component of the spherical tensor operator. There are ve components, starting with the 2 elements,

$$\begin{aligned}\hat{T}_2^{(2)} &= \hat{d}^x \hat{d}^y \\ &= \frac{1}{2} \frac{1}{f} \frac{f+1}{f} \frac{f^0+1}{f} \frac{2f+1}{f(f+1)} \frac{f}{f} \frac{f^0}{f} \\ &\quad + \frac{1}{f+1} \frac{f}{f} \frac{1}{f} \frac{f^0}{f} \frac{1}{f} \hat{f}^2\end{aligned}\quad (\text{A 22})$$

which are quadratic in the atom ic raising and lowering operators. The terms of order 1,

$$\hat{T}^{(2)} = \frac{1}{2} \hat{d}^x \hat{d}_0^y + \hat{d}_0^x \hat{d}^y \quad (\text{A 23})$$

$$\begin{aligned}&= \frac{1}{f} \frac{f}{f} \frac{1}{f} \frac{f^0+1}{f} \frac{2f+1}{f(f+1)} \frac{f}{f} \frac{f^0}{f} \\ &\quad + \frac{1}{f+1} \frac{f+1}{f} \frac{f^0}{f} \frac{1}{f} \hat{f}^x \hat{f}_z^y \frac{1}{2} \hat{\mathbb{1}}_f\end{aligned}$$

couple the light eld to the atom ic operators, $\hat{f}^x \hat{\mathbb{1}}_f$ and $\hat{f}^y \hat{f}_z^y$. Finally, the zero-order term ,

$$\begin{aligned}\hat{T}_0^{(2)} &= \hat{d}_+^x \hat{d}_0^y + 2\hat{d}_0^x \hat{d}_0^y + \hat{d}^x \hat{d}_+^y \\ &= \frac{1}{6} \frac{h}{(f+1)} \frac{f}{f} \frac{1}{f} \frac{f^0+1}{f} (2f+1) \frac{f}{f} \frac{f^0}{f} \\ &\quad + f \frac{f+1}{f} \frac{f^0}{f} \frac{1}{f} \frac{i}{f(f+1)} \frac{3}{\hat{f}_z^2} \hat{f}_z^2 \hat{\mathbb{1}}_f\end{aligned}\quad (\text{A 24})$$

couple the light eld to the atom ic operators, \hat{f}_z^2 and $\hat{\mathbb{1}}_f$. As before, we need to expand the tensor components into the outer product of spherical tensor basis vectors,

$$\begin{aligned}\hat{\epsilon}^{(2)} &= \epsilon_{ijk} \epsilon_{0000}^{q^0 q^1 q^2 q^3} \hat{T}_{q^0 q^1 q^2 q^3}^{(2)} \\ &= \frac{1}{2} \epsilon_{ijk} \epsilon_{0000}^{q^0 q^1 q^2 q^3} \hat{T}_{+2}^{(2)} + \hat{T}_2^{(2)} \frac{2}{3} \hat{T}_0^{(2)} \\ &\quad + i \hat{T}_{+2}^{(2)} \hat{T}_2^{(2)} \frac{q^2}{3} \hat{T}_0^{(2)} \frac{1}{3} \hat{T}_+^{(2)} \hat{T}_+^{(2)} \frac{1}{3} \hat{T}_0^{(2)} \\ &= \epsilon_{ijk} \epsilon_{0000}^{q^0 q^1 q^2 q^3} \hat{T}_{+2}^{(2)} + \hat{T}_2^{(2)} + \frac{2}{3} \hat{T}_0^{(2)} \frac{1}{3} \hat{T}_+^{(2)} + \hat{T}_+^{(2)} \frac{8}{3} \hat{T}_0^{(2)} \\ &\quad + i \hat{T}_{+2}^{(2)} + \hat{T}_2^{(2)} \frac{1}{2} \hat{\mathbb{1}}_f \\ &= \epsilon_{ijk} \epsilon_{0000}^{q^0 q^1 q^2 q^3} \hat{T}_{+2}^{(2)} + \hat{T}_2^{(2)} + \frac{1}{2} \hat{\mathbb{1}}_f + \frac{1}{2} \hat{\mathbb{1}}_f + \frac{1}{6} \frac{h}{f;f^0} \epsilon_{+}^{(2)} \epsilon_{+}^{(2)} \hat{f}_+^2 + \epsilon_{+}^{(2)} \epsilon_{+}^{(2)} \hat{f}_+^2 \hat{f}_z^2 + \epsilon_{+}^{(2)} \epsilon_{+}^{(2)} \hat{f}_z^2 + \epsilon_{+}^{(2)} \epsilon_{+}^{(2)} \hat{f}_z^2 \hat{f}_z^2 + \epsilon_{+}^{(2)} \epsilon_{+}^{(2)} \hat{f}_z^2 \hat{f}_z^2 \hat{\mathbb{1}}_f\end{aligned}\quad (\text{A 25})$$

where ϵ_{ijk} is the completely symmetric tensor (the rank-4 analog of the Levi-Civita symbol), and the rank-2 coe cients are given by,

$$\epsilon_{f;f^0}^{(2)} = \frac{1}{f} \frac{f+1}{f} \frac{f^0+1}{f} \frac{2f+1}{f(f+1)} \frac{f}{f} \frac{f^0}{f} + \frac{1}{f+1} \frac{f}{f} \frac{1}{f} \frac{f^0}{f} \frac{1}{f} : \quad (\text{A 26})$$